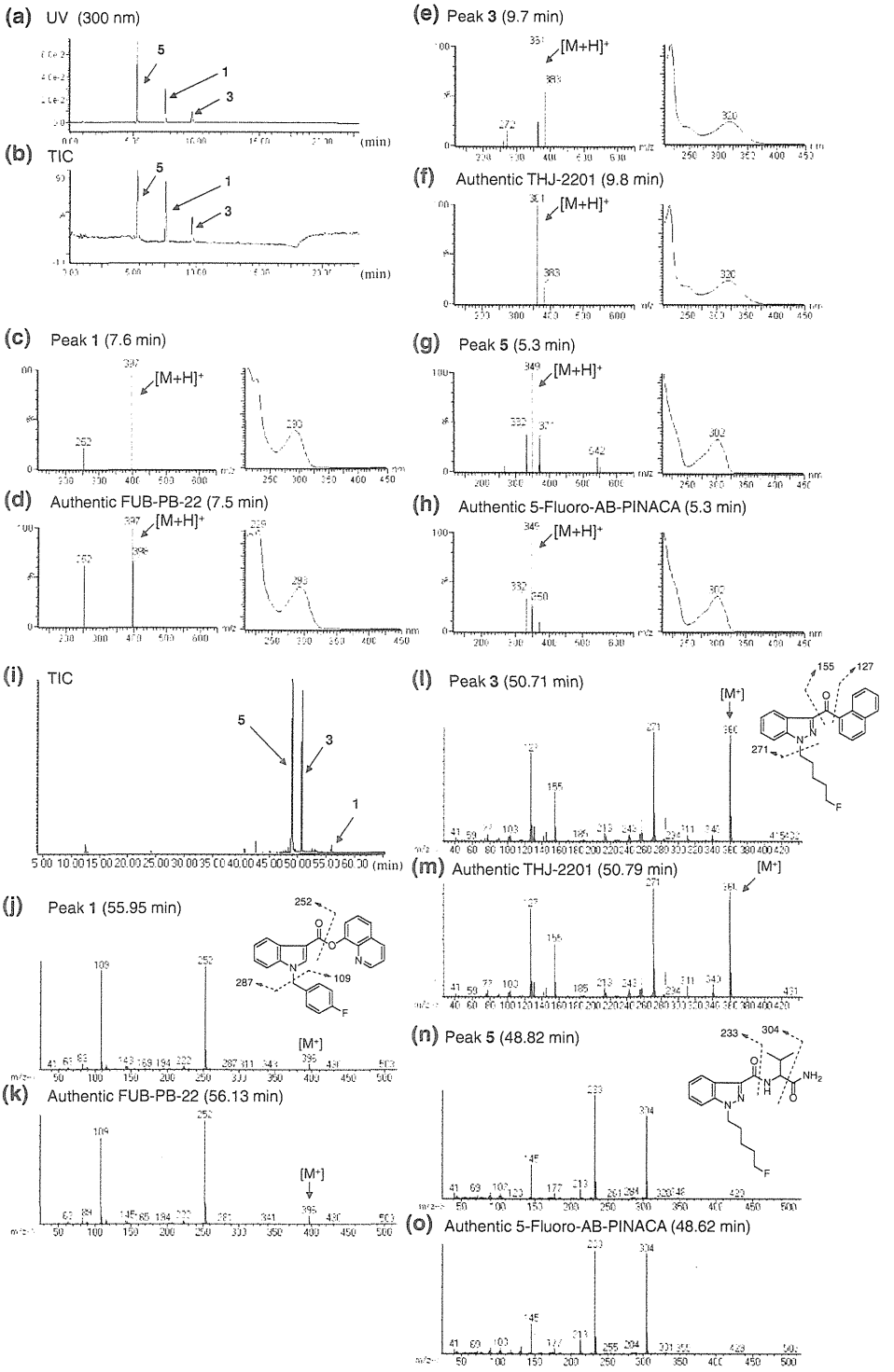

Fig. 2 Liquid chromatography–mass spectrometry (LC–MS) and gas chromatography–mass spectrometry (GC–MS) analyses of product A. The LC–ultraviolet photodiode array (LC–UV-PDA) chromatogram (**a**) and total ion chromatogram (TIC) (**b**) are shown. Electrospray ionization (ESI) mass and UV spectra of peaks **1** (**c**), **3** (**e**), **5** (**g**), the authentic FUB-PB-22 (**d**), AM-2201 indazole analog (THJ-2201, **f**), and 5-fluoro-AB-PINACA (**h**) are also presented. Panels (**i**) through (**o**) show TIC (**i**) and electron ionization (EI) mass spectra of peaks **1** (**j**), **3** (**l**), **5** (**n**), the authentic FUB-PB-22 (**k**), AM-2201 indazole analog (THJ-2201, **m**), and 5-fluoro-AB-PINACA (**o**) obtained by GC–MS analysis

Results and discussion

Identification of unknown peaks 1, 3, and 5

LC–MS and GC–MS analyses were performed to identify unknown peaks **1**, **3**, and **5** in product A (Fig. 2a, b, i). Based on the LC–MS and GC–MS data, the three peaks were finally identified as synthetic cannabinoids; namely, FUB-PB-22 (Fig. 2c, j), an AM-2201 indazole analog (THJ-2201) (Fig. 2e, l), and 5-fluoro-AB-PINACA (Fig. 2g, n), by direct comparison of the data to those of the purchased authentic compounds (Fig. 2d, k; Fig. 2f, m; Fig. 2h, o), respectively. Compounds **1**, **3**, and **5** were detected as newly distributed designer drugs in Japan. These compounds are analogs of known cannabimimetic substances, QUPIC (PB-22) [6], AM-2201, and AB-PINACA [4], respectively, the pharmacological effects for which have not been reported. In addition, FUB-PB-22 (**1**) and 5-fluoro-AB-PINACA (**5**) will be controlled as *Shitei-Yakubutsu* (designated substances) in Japan from July 2014.

Identification of unknown peaks 2 and 4

Two unknown peaks **2** and **4** were detected along with 5-fluoro-AB-PINACA (**5**) in the LC–MS and GC–MS chromatograms for product B (Fig. 3a, b, g). Peaks **2** and **4** were identified as the synthetic cannabinoids 5-fluoro-NNEI indazole analog (5-fluoro-MN-18) (Fig. 3c, h) and XLR-12 (Fig. 3e, j) by direct comparison of the data to those of the purchased authentic compounds (Fig. 3d, i; Fig. 3f, k), respectively. 5-Fluoro-NNEI indazole analog (**2**) is an analog of a known NNEI indazole analog (MN-18), which has already been detected in illegal products [11]. Although there is no pharmacological information about compound **2**, a cyclopropylmethanone-type XLR-12 (**4**), which is an analog of XLR-11, has been reported to show affinity for the cannabinoid CB_1 and CB_2 receptors (K_i = 10 and 0.09 nM, respectively) [13]. In addition, 5-fluoro-NNEI indazole analog (5-fluoro-MN-18, **2**) and XLR-12 (**4**) will be controlled as designated substances in Japan from July 2014.

Identification of unknown peak 6

An unknown peak **6** was detected along with the 5-fluoro-AB-PINACA (**5**) peak in the LC–MS and GC–MS chromatograms for product C (Fig. 4a–c, f). Based on the GC–MS and LC–MS data, the unknown peak **6** was finally identified as dicarboxamide derivative 5-chloro-AB-PINACA (Fig. 4d, g) by direct comparison of the data to those of the purchased authentic compound (Fig. 4e, h). This is the first report of the detection of 5-chloro-AB-PINACA (**6**) as a newly distributed illegal drug in Japan.

Identification of unknown peaks 7 and 8

In the LC–MS and GC–MS analyses, unknown peaks **7** and **8** were detected with FUB-PB-22 (**1**) in product D (Fig. 5a, b, g). Peaks **7** and **8** were identified as synthetic cannabinoids AB-CHMINACA (Fig. 5c, h) and 5-fluoro-AMB (Fig. 5e, j), respectively, by direct comparison of the data to those of the purchased authentic compounds (Fig. 5d, i; Fig. 5f, k). The *S*-form of the dicarboxamide derivative AB-CHMINACA (*N*-[(1*S*)-1-(aminocarbonyl)-2-methylpropyl]-1-(cyclohexylmethyl)-1*H*-indazole-3-carboxamide, **7**) has been reported to have a potent affinity for the cannabinoid CB_1 receptor (K_i = 0.5 nM) [14]. Although there is no pharmacological information about 5-fluoro-AMB (methyl 2-[1-(5-fluoropentyl)-1*H*-indazole-3-carboxamido]-3-methylbutanoate, **8**), its analog, methyl 2-[1-(4-cyanobutyl)-1*H*-indazole-3-carboxamido]-3,3-dimethylbutanoate, has been reported to have a potent affinity for cannabinoid CB_1 receptor (K_i = 0.7 nM) [14].

Identification of the unknown peaks 9 and 12

We detected two unknown peaks, **9** and **12**, in the LC–MS and GC–MS chromatograms for product E (Fig. 6a, b, f). Peak **12** was identified as the cathinone derivative 4′-methoxy-α-pyrrolidinoheptanophenone (4-methoxy-α-PHPP) (Fig. 6d, h) by direct comparison of the data with those of the purchased authentic compound (Fig. 6e, i). 4-Methoxy-α-PHPP (**12**) is a *para*-methoxy analog of a known α-PHPP [11]. The pharmacological and toxicological properties of **12** are not known. Compound **12** was detected as a newly distributed designer drug in Japan. In the LC–MS analysis, the unknown peak **9** at 14.8 min showed a protonated molecular ion signal at *m/z* 266 ($[M+H]^+$) (Fig. 6c). The accurate mass spectrum obtained by LC–QTOF-MS gave an ion peak at *m/z* 266.1746, suggesting that the protonated molecular formula of compound **9** was $C_{15}H_{24}NO_3$ (calcd. 266.1756).

The ^1H and ^{13}C NMR data (Table 1) and the observed DQF-COSY, HMQC, HMBC, and ^{15}N HMBC correlations shown in Fig. 7a revealed that the structure of compound **9** is 1-(3,4-dimethoxyphenyl)-2-(ethylamino)pentan-1-one (DL-4662), as shown in Fig. 1. The fragment ions at *m/z* 100, 137, and 165 of compound **9** in the GC–MS spectrum (Fig. 6g) further confirmed the structure. Compound **9**, which is a dimethoxy-analog of a known cathinone derivative, α-ethylaminopentiophenone [11], is a novel illegal drug, and its chemical and pharmacological data have not been reported.

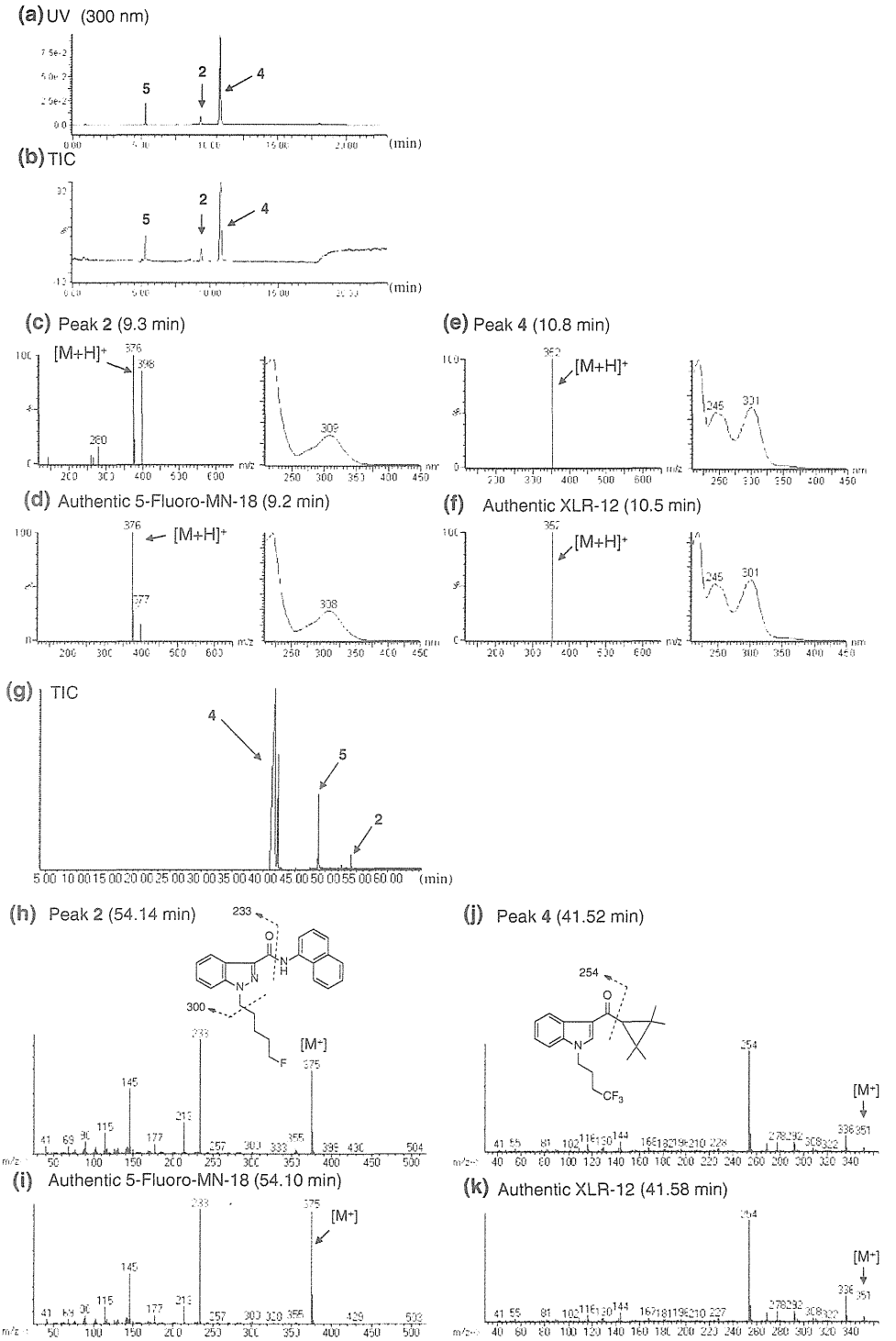

Fig. 3 LC–MS and GC–MS analyses of product B. Panels (**a**) and (**b**) show LC–UV-PDA chromatogram (**a**) and TIC (**b**). ESI mass and UV spectra of peaks **2** (**c**), **4** (**e**), and the authentic 5-fluoro-NNEI indazole analog (**d**) and XLR-12 (**f**) are also shown. Panels (**g**) through (**k**) show TIC (**g**) and EI mass spectra of peaks **2** (**h**), **4** (**j**), and the authentic 5-fluoro-NNEI indazole analog (**i**) and XLR-12 (**k**) obtained by the GC–MS analysis

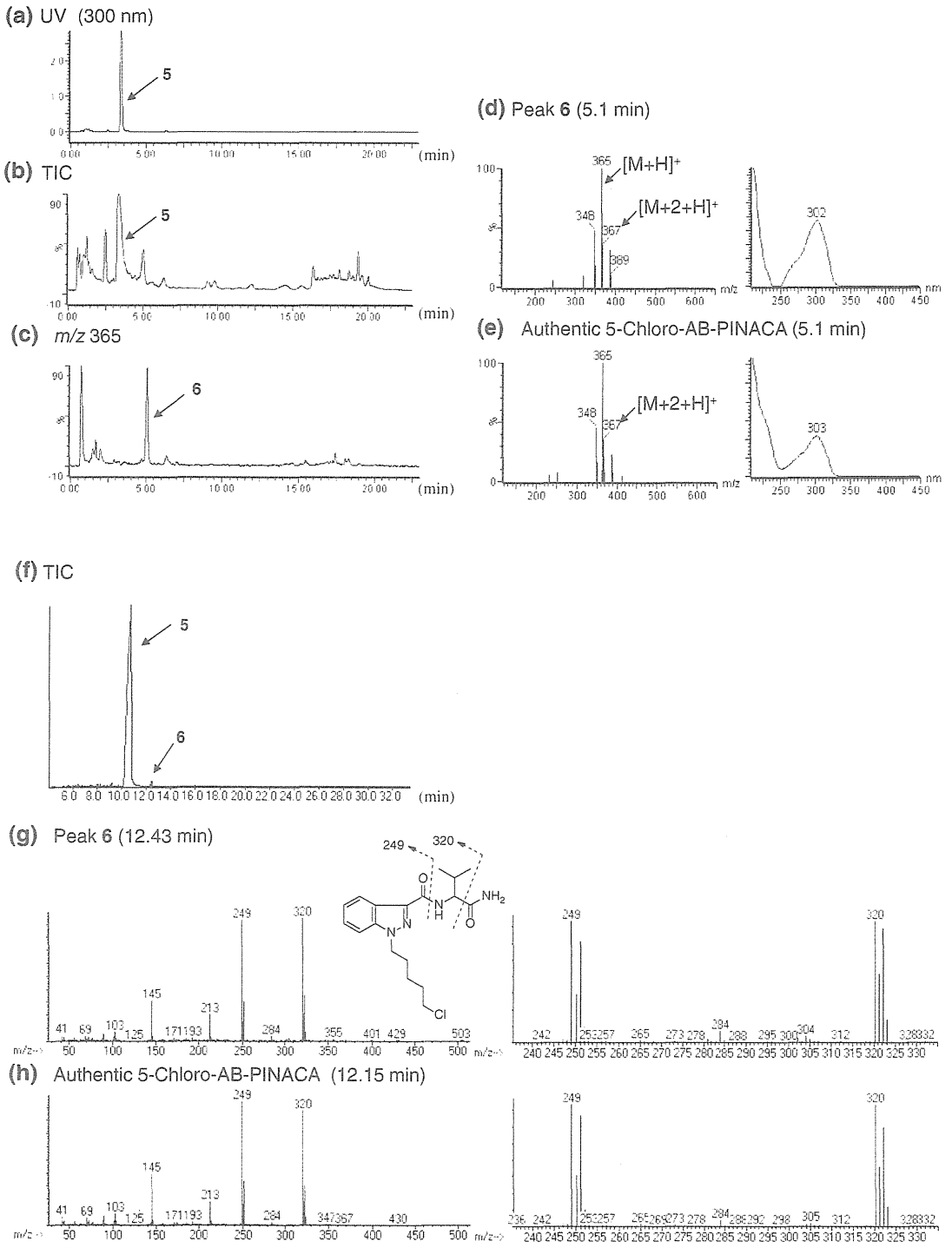

Fig. 4 LC–MS and GC–MS analyses of product C. LC–UV-PDA chromatogram (**a**), TIC (**b**), mass chromatogram at *m/z* 365 (**c**), and ESI mass and UV spectra of peak **6** (**d**) and the authentic 5-chloro-AB-PINACA (**e**) are shown. TIC (**f**) and EI mass spectra of peak **6** (**g**) and the authentic 5-chloro-AB-PINACA (**h**) obtained by GC–MS analysis are also presented

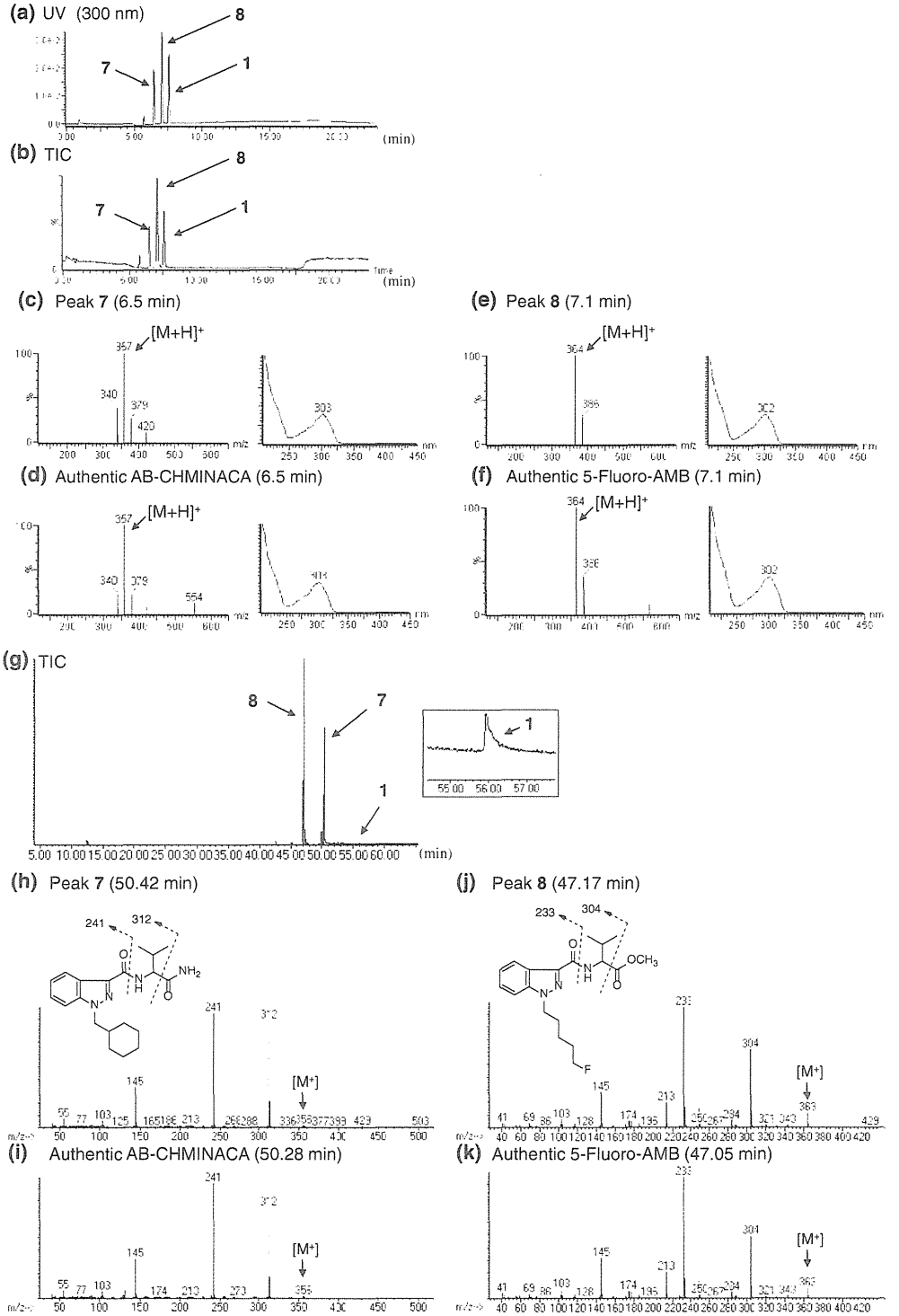

Fig. 5 LC–MS and GC–MS analyses of product D. The LC–UV-PDA chromatogram (**a**) and TIC (**b**) are shown. ESI mass and UV spectra of peaks **7** (**c**), **8** (**e**), and the authentic AB-CHMINACA (**d**) and 5-fluoro-AMB (**f**) are also shown. Panels (**g**) through (**k**) present the TIC (**g**) and EI mass spectra of peaks **7** (**h**), **8** (**j**), and the authentic AB-CHMINACA (**i**) and 5-fluoro-AMB (**k**) obtained by GC–MS analysis

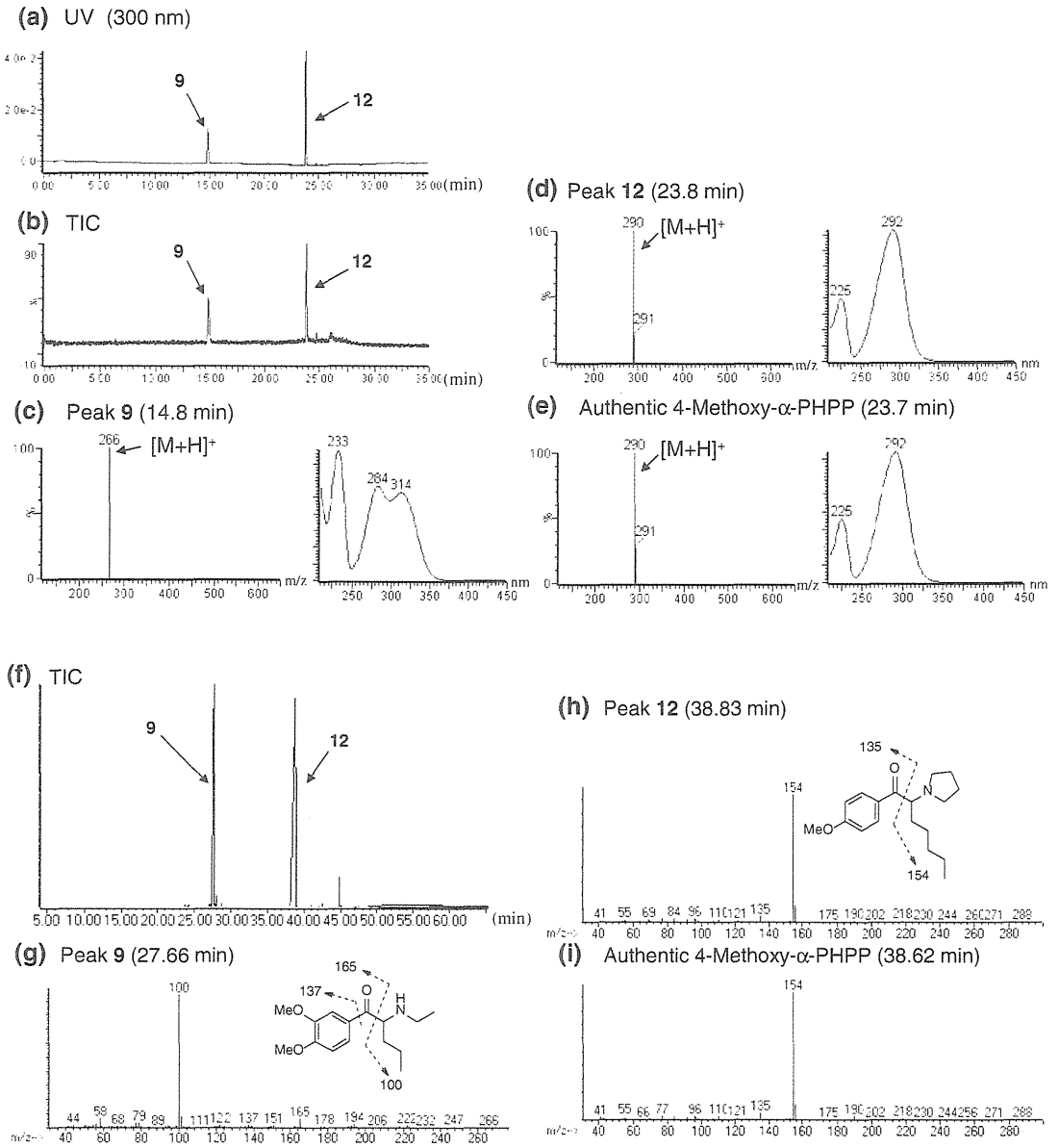

Fig. 6 LC–MS and GC–MS analyses of product E. The LC–UV-PDA chromatogram (**a**) and TIC (**b**) are shown, along with the ESI mass and UV spectra of peaks **9** (**c**), **12** (**d**), and the authentic 4-methoxy-α-PHPP (**e**). Panels (**f**) through (**i**) show TIC (**f**) and EI mass spectra of peaks **9** (**g**), **12** (**h**), and the authentic 4-methoxy-α-PHPP (**i**) obtained by GC–MS analysis

Identification of the unknown peaks **10** and **13**

Unknown peaks **10** and **13** were detected along with a peak for known compound 25B-NBOMe [10] in the LC–MS and GC–MS chromatograms for product F (Fig. 8a, b, f). Based on the GC–MS and LC–MS data, peak **13** was finally identified as the cathinone derivative 4′- fluoro-α-pyrrolidinoheptanophenone (4-fluoro-α-PHPP) (Fig. 8d, h) by direct comparison of the data to those of the purchased authentic compound (Fig. 8e, i). In the LC–MS analysis, unknown peak **10** at 19.0 min showed a protonated molecular ion signal at *m/z* 246 ($[M+H]^+$) (Fig. 8c). The accurate mass spectrum obtained by LC–QTOF-MS gave an ion peak at *m/z* 246.1840, suggesting that the protonated molecular formula of compound **10** was $C_{16}H_{24}NO$ (calcd. 246.1858).

The ^{1}H and ^{13}C NMR spectra of compound **10** were very similar to those of a known cathinone derivative, α-POP, except for the additional C_2H_4 of the *n*-alkyl moiety (positions 5 and 6) of α-POP, as shown in Tables 2 and 3 [11]. The observed ^{1}H and ^{13}C NMR data (Tables 2, 3) and DQF-COSY, HMQC, HMBC, and ^{15}N HMBC correlations

(data not shown) revealed that the structure of compound **10** corresponded to α-pyrrolidinohexylphenone (α-PHP), as shown in Fig. 1. The fragment ions at *m/z* 77, 105, and 140 of compound **10** in the GC–MS spectrum (Fig. 8g) further confirmed the structure. Compound **10** is a desmethyl analog of MPHP, which is controlled as a designated substance in Japan, and its chemical and pharmacological data have not been reported.

Identification of unknown peak 11

Unknown peak **11** was detected in the GC–MS and LC–MS chromatograms for product G (Fig. 9a, b, d). The proposed fragmentation and the presumed structure of peak **11** obtained by GC–MS analysis are shown in Fig. 9e. The LC–MS data revealed that peak **11** gave a protonated ion signal at *m/z* 304 ($[M+H]^+$) (Fig. 9c). The accurate mass spectrum obtained by LC–QTOF-MS gave an ion peak at *m/z* 304.2269, suggesting that the protonated molecular formula of compound **11** was $C_{19}H_{30}NO_2$ (calcd. 304.2269).

The ^{13}C NMR spectrum of compound **11** was similar to that of α-POP except for the C-1′ and C-3′ to C-5′ carbons of a phenyl group and the 4′-methoxy carbon (Table 2) [11]. The observed ^1H and ^{13}C NMR data (Tables 2, 3) and DQF-COSY, HMQC, HMBC, and ^{15}N HMBC correlations (data not shown) suggested that the structure of compound **11** is 4′-methoxy-α-pyrrolidinooctanophenone (4-methoxy-α-POP), as shown in Fig. 1. The fragment ions at *m/z* 135 and 168 of compound **11** in the GC–MS spectrum corroborated the structure (Fig. 9e). Compound **11** was detected as a newly distributed designer drug, and its chemical and pharmacological data have not been reported.

Table 1 Nuclear magnetic resonance (NMR) data of DL-4662 (**9**)

No	^{13}C	^1H
1	195.1	–
2	62.5	5.12, 1H, t, J = 5.5 Hz
3	34.4	1.94, 2H, m
4	18.8	1.35, 1H, m, overlapped
		1.26, 1H, m
5	14.2	0.90, 3H, t, J = 7.3 Hz
1′	128.2	–
2′	111.8	7.57, 1H, d, J = 1.8 Hz
3′	151.1	–
4′	156.7	–
5′	112.0	7.12, 1H, d, J = 8.3 Hz
6′	125.4	7.74, 1H, dd, J = 8.3, 2.3 Hz
1″	43.3	3.08 and 3.00, each 1H, m
2″	11.8	1.34, 3H, t, J = 7.3 Hz, overlapped
3′-OMe	56.5	3.90, 3H, s
4′-OMe	56.7	3.94, 3H, s

Spectra recorded in methanol-d_4 at 800 MHz (^1H) and 200 MHz (^{13}C); data in δ ppm; *OMe* methoxy

Identification of unknown peak 14

We detected unknown peak **14** in the LC–MS and GC–MS chromatograms for product H (Fig. 10a, b, d). In LC–MS analysis, unknown peak **14** at 15.5 min showed a protonated molecular ion signal at *m/z* 204 ($[M+H]^+$) (Fig. 10c). The accurate mass spectrum obtained by LC–QTOF-MS gave an ion peak at *m/z* 204.1377, suggesting that the protonated molecular formula of compound **14** was $C_{13}H_{18}NO$ (calcd. 204.1388).

The structure of compound **14** was elucidated by NMR analysis (Fig. 7b; Table 4). The ^1H and ^{13}C NMR spectra of compound **14** suggested the existence of 17 protons and 13 carbons (Table 4). Interpretation of DQF-COSY, HMQC, and HMBC spectra of compound **14** revealed the presence of a 2-propylbenzofuran moiety (positions 2 to 7a and position 1′ to 3′, Fig. 7b). The remaining C_2H_6N unit was presumed to be an *N*-ethylamine group. In addition,

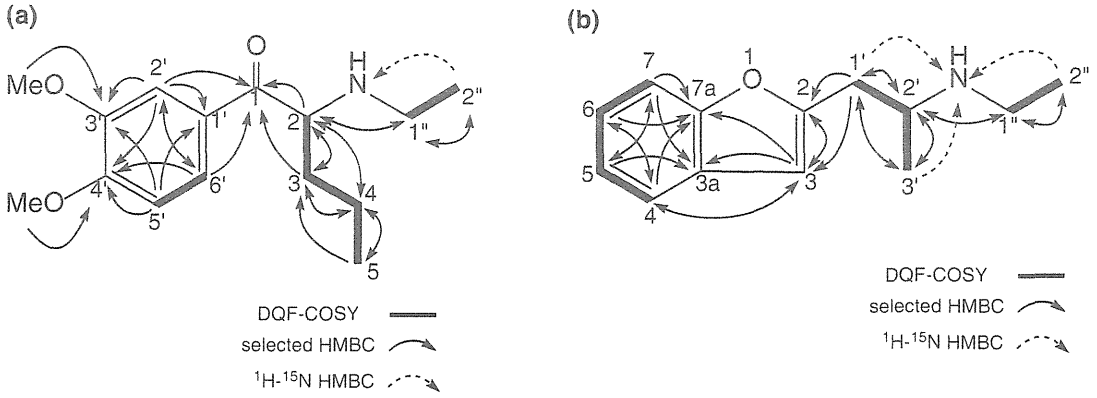

Fig. 7 Double quantum filtered correlation spectroscopy (DQF-COSY), selected heteronuclear multiple-bond correlation (HMBC), and ^1H–^{15}N HMBC correlations for compound **9** (DL-4662, **a**), and for compound **14** (2-EAPB, **b**)

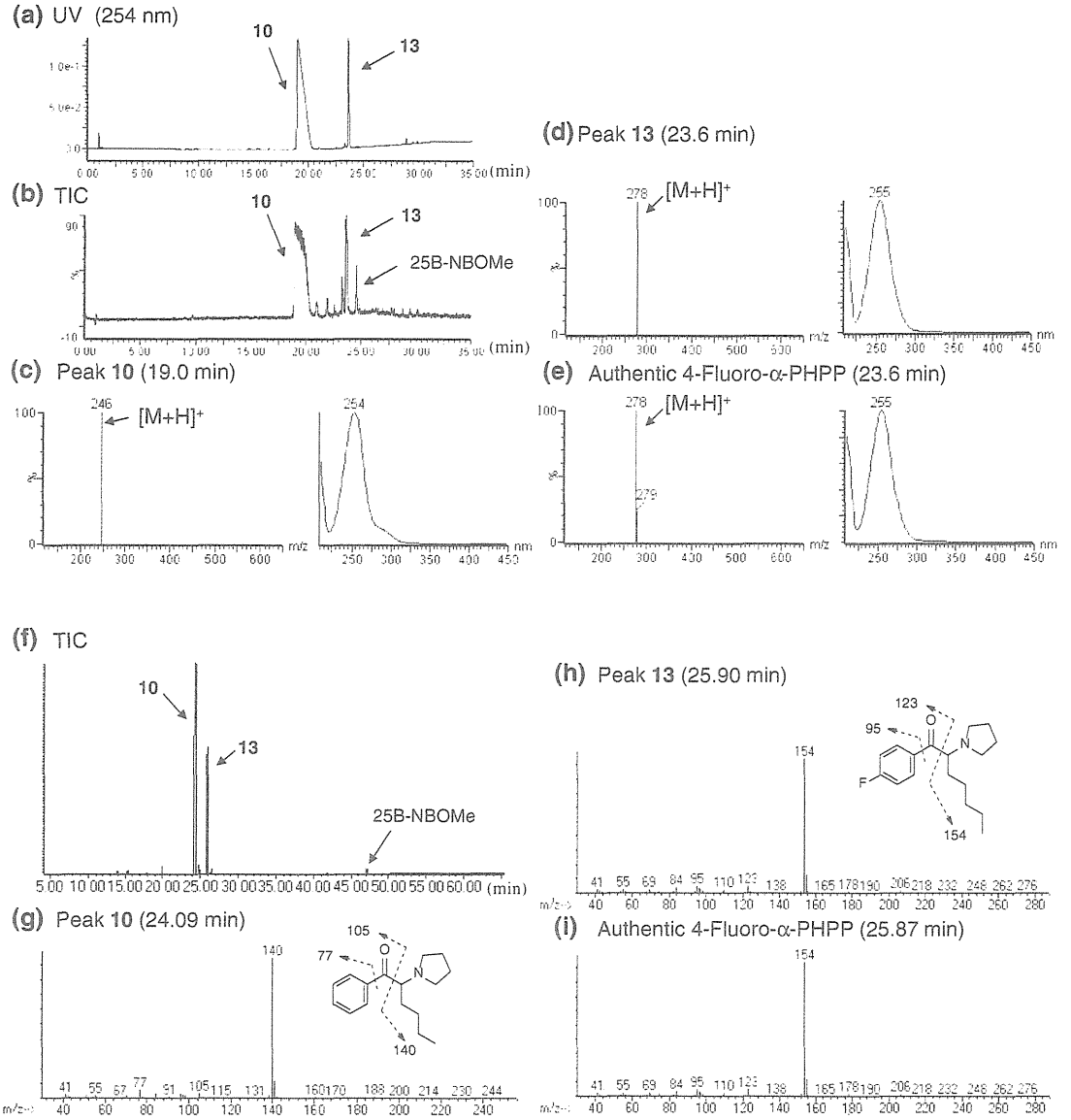

Fig. 8 LC–MS and GC–MS analyses of product F. The LC–UV-PDA chromatogram (**a**) and TIC (**b**) are shown, along with ESI mass and UV spectra of peaks **10** (**c**), **13** (**d**), and the authentic 4-fluoro-α-PHPP (**e**). Panels (**f**) through (**i**) show TIC (**f**) and EI mass spectra of peaks **10** (**g**), **13** (**h**), and the authentic 4-fluoro-α-PHPP (**i**) obtained by GC–MS analysis

^{15}N HMBC correlations between NH and each of H-1′, H-3′, and H-2″, and an HMBC correlation between a methine (position 2′) and a methylene (position 1″) were observed (Fig. 7b). These results revealed that a 2-propylbenzofuran moiety was connected at position 2′ to the *N*-ethylamine group at nitrogen (Fig. 7b). Therefore, the structure of compound **14** was clarified as a benzofuran derivative, 2-(2-ethylaminopropyl)benzofuran (2-EAPB), as shown in Fig. 1. Compound **14** was detected as a newly distributed designer drug, and its pharmacological data have not been reported. However, the benzofuran derivatives 5-APB [5-(2-aminopropyl)benzofuran] and 6-APB [6-(2-aminopropyl)benzofuran] have been reported as potent triple monoamine reuptake inhibitors for dopamine, norepinephrine, and serotonin in vitro [15]. In addition, it has been reported that the 2-ethylaminopropyl regioisomer of **14**, 5-EAPB [5-(2-ethylaminopropyl)benzofuran], is offered for sale as an alternative to other benzofurans in the UK [16].

Identification of the unknown peaks 15–19

GC–MS and LC–MS analyses were performed to identify the five unknown peaks **15**, **16**, **17**, and **18** and **19** in

Table 2 ^{13}C NMR data of compounds **10** and **11** and α-POP

No.	α-PHP (**10**)	α-POP [a]	4-MeO-α-POP (**11**)
1	198.0	198.7	196.7
2	66.8	66.8	66.9
3	30.2	30.1	30.7
4	27.9	26.2	26.0
5	22.8	29.5	29.5
6	13.7	31.6	31.6
7	–	22.7	22.7
8	–	14.1	14.1
1′	136.5	137.0	130.0
2′/6′	129.4	129.2	131.9
3′/5′	129.5	129.3	114.7
4′	134.7	134.2	164.8
2″/5″	52.0	51.3	51.7
3″/4″	24.0	24.0	23.9
4′-OMe	–	–	55.7

Spectra recorded at 200 MHz in pyridine-d_5

4-MeO-α-POP 4-methoxy-α-POP

[a] Data from Uchiyama et al. [11]

Table 3 ^{1}H NMR data of compounds **10** and **11** and α-POP

No.	α-PHP (**10**)	α-POP [a]	4-MeO-α-POP (**11**)
1	–	–	–
2	5.59, 1H, brs	5.03, 1H, brs	5.42, 1H, brs
3	2.18, 2H, m	2.11, 2H, m	2.17, 2H, m
4	1.42, 1H, m	1.37, 2H, m	1.38, 2H, m
	1.31, 1H, m	–	–
5	1.11, 2H, m	1.12, 2H, m, overlapped	1.12, 2H, m, overlapped
6	0.65, 3H, t, J = 7.3 Hz	1.02, 2H, m, overlapped	1.02, 2H, m, overlapped
7	–	1.08, 2H, m, overlapped	1.07, 2H, m, overlapped
8	–	0.72, 3H, t, J = 7.6 Hz	0.70, 3H, t, J = 7.3 Hz
1′	–	–	–
2′/6′	8.35, 2H, dd, J = 8.2, 0.8 Hz	8.33, 2H, dd, J = 8.6, 1.4 Hz	8.44, 2H, d, J = 8.7 Hz
3′/5′	7.51, 2H, t, J = 7.8 Hz	7.50, 2H, t, J = 8.6 Hz	7.09, 2H, t, J = 8.7 Hz
4′	7.59, 1H, t, J = 7.3 Hz	7.58, 1H, tt, J = 8.6, 1.4 Hz	–
2″/5″	3.53, 3.39, each 2H, brs	3.28, 3.10, each 2H, brs	3.44, 3.30, each 2H, brs
3″/4″	1.95, 1.89, each 2H, m	1.80, 4H, m	1.88, 1.84, each 2H, m
4′-OMe	–	–	3.71, 3H, s

Spectra recorded at 800 MHz in pyridine-d_5; data in δ ppm

[a] Data from Uchiyama et al. [11]

products I (Supplementary material, Fig. S1a, b, e), J (Fig. S2a–d, g), K (Fig. S3a–d, i), and L (Fig. S4a, b, e), respectively. Based on the GC–MS and LC–MS data, the five peaks were finally identified as nitracaine (Fig. S1c, f), diclofensine (Fig. S2e, h), diphenidine (Fig. S3e, j), 1-benzylpiperidine (Fig. S3g, l), and acetylfentanyl (Fig. S4c, f), respectively, by direct comparison of the data with those of the purchased authentic compounds (Fig. S1d, g; Fig. S2f, i; Fig. S3f, k; Fig. S3h, m; Fig. S4d, g). Researchers in Ireland reported that nitracaine (**15**), which is the nitro analog of the local anesthetic dimethocaine, emerged in December 2013 as a new psychoactive substance on an Internet website selling "research chemicals" [17]. Diclofensine (**16**) has been reported as an inhibitor of monoamine uptake [18], while diphenidine (**17**) has been reported as an *N*-methyl-D-aspartate (NMDA) channel blocker [19]. The opioid receptor agonist acetylfentanyl (**19**) will be controlled as a designated substance in Japan from July 2014.

Combination patterns of detected compounds in illegal products

As described in our previous reports [3, 20], our survey of illegal products distributed in Japan revealed that the average number of synthetic compounds detected per illegal product was 2.6 in 2010–2012. In some cases, synthetic compounds of different types, such as synthetic cannabinoids and cathinone derivatives, were present in the same product [3]. In this study, 34 compounds, including compounds **1**–**19**, were detected in the products, and the detected compounds were categorized into three types: synthetic cannabinoids (10 compounds), cathinone derivatives (13 compounds), and other classes of designer drugs (10 compounds) (Table 5). Table 6 provides a list of the different combination patterns of detected compounds in 104 illegal products purchased between November 2013 and May 2014. Sixty combination patterns were detected, with the number of compounds per product ranging from one to seven: one detected compound (10 patterns), two (23 patterns), three (14 patterns), four (4 patterns), five (6 patterns), six (2 patterns), and seven (1 pattern), as shown in Table 6.

The combination patterns were classified broadly into seven groups (A–G) based on the types of compounds, as shown in Table 6. Group A consisted of a mixture of only synthetic cannabinoid(s) with 17 patterns, group B was a mixture of only cathinone derivative(s) with 11 patterns, group C was a mixture of other compound(s) with 4 patterns, group D was a mixture of synthetic cannabinoid(s) and cathinone derivative(s) with 21 patterns, group E was a mixture of a synthetic cannabinoid and another compound with 1 pattern, group F was a mixture of cathinone

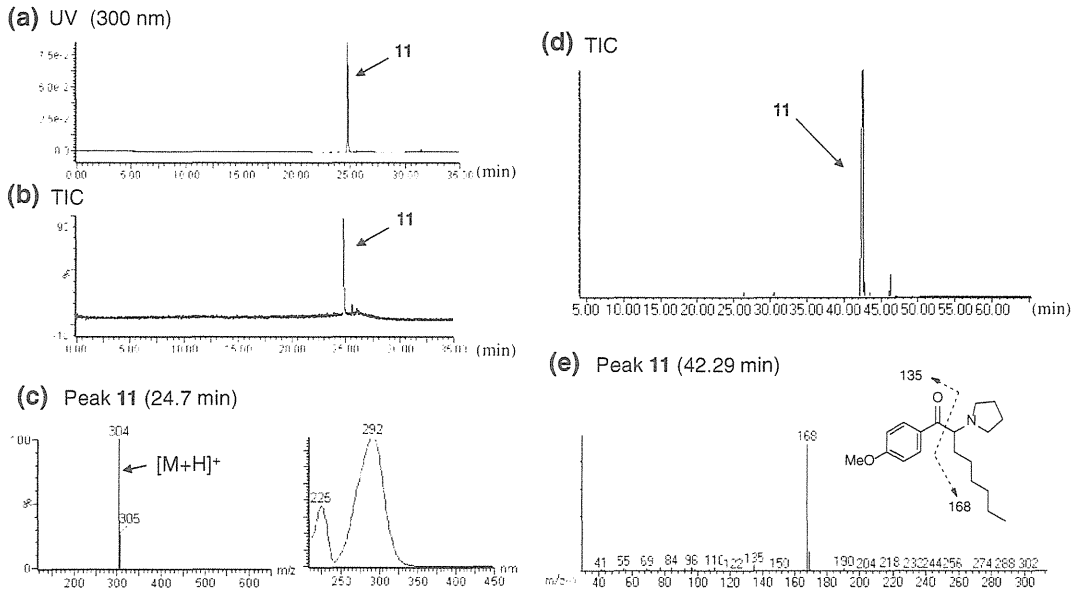

Fig. 9 LC–MS and GC–MS analyses of product G. The LC–UV-PDA chromatogram (**a**), TIC (**b**), and ESI mass and UV spectra of peak **11** (**c**) are shown. TIC (**d**) and EI mass spectra of peak **11** (**e**) obtained by GC–MS analysis are also presented

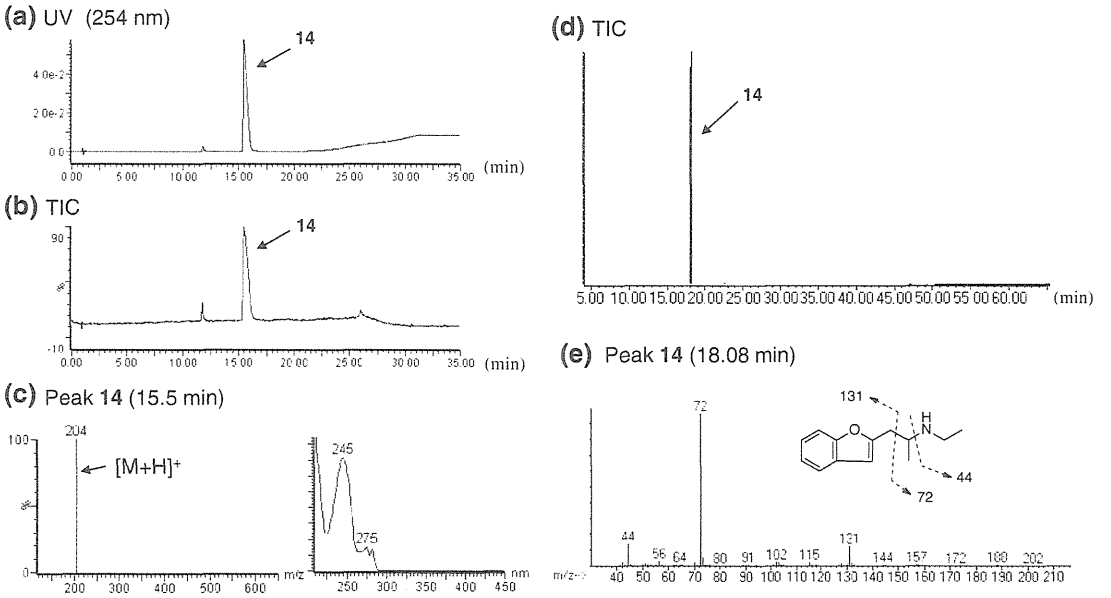

Fig. 10 LC–MS and GC–MS analyses of product H. The LC–UV-PDA chromatogram (**a**), TIC (**b**), and ESI mass and UV spectra of peak **14** (**c**) are presented. Also shown are the TIC (**d**) and EI mass spectra of peak **14** (**e**) obtained by GC–MS analysis

derivative(s) and another compound with 2 patterns, and group G was a mixture of synthetic cannabinoid(s), cathinone derivative(s), and other compound(s) with 4 patterns.

As in the case of group G-(1), the product contained three different types of compounds with different pharmacological effects: the synthetic cannabinoid 5-fluoro-NNEI

Table 4 NMR data of 2-EAPB (**14**)

No.	^{13}C	^{1}H
1	–	–
	153.9	–
3	106.8	6.72, 1H, s
3a	129.8	–
4	121.9	7.55, 1H, d, J = 7.6 Hz
5	124.1	7.21, 1H, t, J = 7.6 Hz
6	125.3	7.27, 1H, t, J = 7.6 Hz
7	111.9	7.45, 1H, d, J = 7.6 Hz
7a	156.5	–
1′	33.0	3.27, 1H, dd, J = 15.0, 5.0 Hz
		3.11, 1H, m, overlapped
2′	53.4	3.68, 1H, m
3′	16.7	1.35, 3H, t, J = 6.9 Hz, overlapped
1″	41.7	3.16, 3.14, each 1H, m, overlapped
2″	11.8	1.33, 3H, t, J = 7.2 Hz, overlapped
NH	–	8.87, 1H, brs [a]

Spectra recorded at 600 MHz (^{1}H) and 150 MHz (^{13}C) in methanol-d_4; data in δ ppm

[a] Recorded in dimethyl sulfoxide-d_6

Table 5 List of detected compounds

Types of compounds	Detected compounds
10 Synthetic cannabinoids	FUB-PB-22 (**1**)
	5-Fluoro-NNEI indazole analog (5-fluoro-MN-18) (**2**)
	AM2201indazole analog (THJ-2201) (**3**)
	XLR-12 (**4**)
	5-Fluoro-AB-PINACA (**5**)
	5-Chloro-AB-PINACA (**6**)
	AB-CHMINACA (**7**)
	5-Fluoro-AMB (**8**)
	NNEI indazole analog (MN-18)
	QUPIC N-(5-fluoropentyl) analog (5-fluoro-PB-22)
13 Cathinone derivatives	DL-4662 (**9**)
	α-PHP (**10**)
	4-Methoxy-α-POP (**11**)
	4-Methoxy-α-PHPP (**12**)
	4-Fluoro-α-PHPP (**13**)
	α-POP
	3,4-Dimethoxy-α-PVP
	4-Ethylmethcathinone
	4-Methoxy-α-PVP
	4-Methylbuphedrone
	4-Methyl-α-ethylaminopentiophenone
	N-Ethylbuphedrone (NEB)
	Pentedrone
10 Other compounds	2-EAPB (**14**)
	Nitracaine (**15**)
	Diclofensine (**16**)
	Diphenidine (**17**)
	1-Benzylpiperidine (**18**)
	Acetyl fentanyl (**19**)
	α-PVT
	25I-NBOMe
	25B-NBOMe
	25N-NBOMe

indazole analog (**2**), the cathinone derivative α-POP, and the NMDA channel blocker diclofensine (**16**). On the other hand, in the case of group G-(2), the product contained the synthetic cannabinoid FUB-PB-22 (**1**), the two cathinone derivatives 4-methyl-α-ethylaminopentiophenone and 3,4-dimethoxy-α-PVP, and the phenethylamine derivative 25I-NBOMe, which is a 5-HT_{2A} receptor agonist with hallucinogenic effects. Considering the results, it is apparent that the types of emerging compounds are becoming more diverse, as are their combinations in illegal products.

Conclusions

Nineteen newly distributed designer drugs, including eight synthetic cannabinoids (**1**–**8**), five cathinone derivatives (**9**–**13**), and six other substances—2-EAPB (**14**), nitracaine (**15**), diclofensine (**16**), diphenidine (**17**), 1-benzylpiperidine (**18**), and acetylfentanyl (**19**)—were identified in illegal products that are available in Japan. Most of the detected compounds (**1**–**14** and **19**) appeared as alternatives to controlled substances such as narcotics and designated substances in Japan. It is apparent that the types of designer drugs and their combinations in illegal products seem to be increasing in diversity. Thus, serious side effects from these combinations are possible, although it is hard to predict them. The emergence of designer drugs that are neither synthetic cannabinoids nor cathinone derivatives also seems to be increasing. Therefore, continuous

Table 6 List of 60 combination patterns of 34 detected compounds in 104 illegal products purchased between November 2013 and May 2014

Nubmer of compound(s) (Number of patterns)	Number of product(s)	Groups of combinations	Detected compound(s)						
1 (10 patterns)	2	A	**5-Fluoro-AB-PINACA**						
	7	A	**FUB-PB-22**						
	3	B	*α-PHP*						
	3	B	*DL-4662*						
	2	B	*4-Fluoro-α-PHPP*						
	2	B	*4-Methoxy-α-PHPP*						
	1	B	*4-Methoxy-α-POP*						
	1	C	Nitracaine						
	4	C	2-EAPB						
	1	C	Acetyl fentanyl						
2 (23 patterns)	7	A	**FUB-PB-22**	**NNEI indazole analog**					
	2	A	**FUB-PB-22**	**AM2201indazole analog (THJ-2201)**					
	4	A	**FUB-PB-22**	**5-Fluoro-AB-PINACA**					
	5	A	**FUB-PB-22**	**5-Fluoro-NNEI indazole analog (5-Fluoro-MN-18)**					
	3	A	**FUB-PB-22**	**QUPIC N-(5-fluoropentyl) analog**					
	3	A	**NNEI indazole analog**	**5-Fluoro-AB-PINACA**					
	1	A	**NNEI indazole analog**	**5-Fluoro-NNEI indazole analog (5-Fluoro-MN-18)**					
	2	A	**QUPIC N-(5-fluoropentyl) analog**	**5-Fluoro-AB-PINACA**					
	1	A	**5-Chloro-AB-PINACA**	**5-Fluoro-AB-PINACA**					
	6	D	**FUB-PB-22**	*DL-4662*					
	2	D	**FUB-PB-22**	*4-Methyl-α-ethylaminopentiophenone*					
	1	D	**FUB-PB-22**	*4-Methylbuphedrone*					
	1	D	**XLR-12**	*α-PHP*					
	1	D	**XLR-12**	*4-Methoxy-α-PHPP*					
	3	E	**5-Fluoro-NNEI indazole analog (5-Fluoro-MN-18)**	2-EAPB					
	1	B	*α-PHP*	*DL-4662*					
	1	B	*α-POP*	*4-Methoxy-α-PHPP*					
	1	B	*α-POP*	*4-Fluoro α-PHPP*					
	1	B	*DL-4662*	*4-Fluoro-α-PHPP*					
	1	B	*DL-4662*	*4-Methoxy-α-PHPP*					
	1	B	*4-Fluoro-α-PHPP*	*4-Methoxy-α-PHPP*					
	1	F	*α-PHP*	25N-NBOMe					
	1	C	Diphenidine	1-Benzylpiperidine					
3 (14 patterns)	1	A	**AB-CHMINACA**	**FUB-PB-22**	**5-Fluoro-AMB**				
	1	A	**AB-CHMINACA**	**NNEI indazole analog**	**5-Fluoro-AMB**				
	2	A	**FUB-PB-22**	**NNEI indazole analog**	**5-Fluoro-AB-PINACA**				
	1	A	**FUB-PB-22**	**NNEI indazole analog**	**5-Fluoro-NNEI indazole analog (5-Fluoro-MN-18)**				
	1	A	**FUB-PB-22**	**AM2201indazole analog (THJ-2201)**	**5-Fluoro-AB-PINACA**				
	1	A	**XLR-12**	**5-Fluoro-AB-PINACA**	**5-Fluoro-NNEI indazole analog (5-Fluoro-MN-18)**				
	1	D	**FUB-PB-22**	**NNEI indazole analog**	*4-Methyl-α-ethylaminopentiophenone*				
	1	D	**FUB-PB-22**	**NNEI indazole analog**	*4-Methoxy-α-PHPP*				
	1	D	**5-Fluoro-AMB**	*α-PHP*	*DL-4662*				
	1	D	**FUB-PB-22**	*4-Methyl-α-ethylaminopentiophenone*	*3,4-Dimethoxy-α-PVP*				
	1	D	**FUB-PB-22**	*4-Methyl-α-ethylaminopentiophenone*	*4-Methoxy-α-PVP*				
	1	D	**XLR-12**	*4-Fluoro-α-PHPP*	*4-Methoxy-α-PHPP*				
	1	G-(1)	**5-Fluoro-NNEI indazole analog (5-Fluoro-MN-18)**	*α-POP*	Diclofensine				
	1	F	*α-PHP*	*4-Fluoro-α-PHPP*	25B-NBOMe				
4 (4 patterns)	1	D	**FUB-PB-22**	**NNEI indazole analog**	*3,4-Dimethoxy-α-PVP*	*4-Methoxy-α-PVP*			
	1	D	**FUB-PB-22**	*Pentedrone*	*4-Methyl-α-ethylaminopentiophenone*	*3,4-Dimethoxy-α-PVP*			
	1	G-(2)	**FUB-PB-22**	*4-Methyl-α-ethylaminopentiophenone*	*3,4-Dimethoxy-α-PVP*	25I-NBOMe			
	1	G	**FUB-PB-22**	*4-Methyl-α-ethylaminopentiophenone*	*3,4-Dimethoxy-α-PVP*	*α*-PVT			
5 (6 patterns)	1	D	**AB-CHMINACA**	**NNEI indazole analog**	**AM2201indazole analog (THJ-2201)**	**5-Fluoro-AMB**	*α-PHP*		
	1	D	**AB-CHMINACA**	**AM2201indazole analog (THJ-2201)**	**5-Fluoro-AMB**	*α-PHP*	*DL-4662*		
	1	D	**FUB-PB-22**	**NNEI indazole analog**	*Pentedrone*	*4-Methylbuphedrone*	*4-Methyl-α-ethylaminopentiophenone*		
	1	D	**FUB-PB-22**	*N-Ethylbuphedrone (NEB)*	*4-Methyl-α-ethylaminopentiophenone*	*3,4-Dimethoxy-α-PVP*	*4-Ethylmethcathinone*		
	1	D	**FUB-PB-22**	*4-Methyl-α-ethylaminopentiophenone*	*Pentedrone*	*4-Methoxy-α-PVP*	*4-Methylbuphedrone*		
	1	G	**FUB-PB-22**	*3,4-Dimethoxy-α-PVP*	*4-Ethylmethcathinone*	*4-Methoxy-α-PVP*	*α*-PVT		
6 (2 patterns)	1	D	**AB-CHMINACA**	**FUB-PB-22**	**NNEI indazole analog**	**AM2201indazole analog (THJ-2201)**	**5-Fluoro-AMB**	*DL-4662*	
	1	D	**AB-CHMINACA**	**FUB-PB-22**	**NNEI indazole analog**	**AM2201indazole analog (THJ-2201)**	**5-Fluoro-AMB**	*α-PHP*	
7 (1 pattern)	1	D	**AB-CHMINACA**	**FUB-PB-22**	**NNEI indazole analog**	**AM2201indazole analog (THJ-2201)**	**5-Fluoro-AB-PINACA**	**5-Fluoro-AMB**	*DL-4662*
(60 patterns)	Total 104								

Synthetic cannabinoids (Bold), *cathinone derivatives (Italic)* and other compounds (Roman)

monitoring and rapid identification of newly distributed designer drugs, combined with global information sharing, will be needed to supress illegal drug abuse.

Acknowledgments Part of this work was supported by a Health and Labor Sciences Research Grant from the Ministry of Health, Labour, and Welfare, Japan.

Conflict of interest There are no financial or other relations that could lead to a conflict of interest.

References

1. Uchiyama N, Kikura-Hanajiri R, Kawahara N, Goda Y (2009) Identification of a cannabimimetic indole as a designer drug in a herbal product. Forensic Toxicol 27:61–66
2. Uchiyama N, Kawamura M, Kikura-Hanajiri R, Goda Y (2012) Identification of two new-type synthetic cannabinoids, *N*-(1-adamantyl)-1-pentyl-1*H*-indole-3-carboxamide (APICA) and *N*-(1-adamantyl)-1-pentyl-1*H*-indazole-3-carboxamide (APINACA), and detection of five synthetic cannabinoids, AM-1220, AM-2233, AM-1241, CB-13 (CRA-13), and AM-1248, as designer drugs in illegal products. Forensic Toxicol 30:114–125
3. Kikura-Hanajiri R, Uchiyama N, Kawamura M, Goda Y (2013) Changes in the prevalence of synthetic cannabinoids and cathinone derivatives in Japan until early 2012. Forensic Toxicol 31:44–53
4. Uchiyama N, Matsuda S, Wakana D, Kikura-Hanajiri R, Goda Y (2013) New cannabimimetic indazole derivatives, *N*-(1-amino-3-methyl-1-oxobutan-2-yl)-1-pentyl-1*H*-indazole-3-carboxamide (AB-PINACA) and *N*-(1-amino-3-methyl-1-oxobutan-2-yl)-1-(4-fluorobenzyl)-1*H*-indazole-3-carboxamide (AB-FUBINACA), identified as designer drugs. Forensic Toxicol 31:93–100
5. Takahashi K, Uchiyama N, Fukiwake T, Hasegawa T, Saijou M, Motoki Y, Kikura-Hanajiri R, Goda Y (2013) Identification and quantitation of JWH-213, a cannabimimetic indole, as a designer drug in a herbal product. Forensic Toxicol 31:145–150
6. Uchiyama N, Matsuda S, Kawamura M, Kikura-Hanajiri R, Goda Y (2013) Two new-type cannabimimetic quinolinyl carboxylates, QUPIC and QUCHIC, two new cannabimimetic carboxamide derivatives, ADB-FUBINACA and ADBICA, and five synthetic cannabinoids detected with a thiophene derivative α-PVT and an opioid receptor agonist AH-7921 identified in illegal products. Forensic Toxicol 31:223–240
7. UNODC (2014) 2014 Global synthetic drugs assessment. Amphetamine-type stimulants and new psychoactive substances, May 2014. http://www.unodc.org/documents/scientific/2014_Global_Synthetic_Drugs_Assessment_web.pdf. Accessed May 2014
8. EMCDDA (2014) European drug report 2014: trends and developments, May 2014. http://www.emcdda.europa.eu/attachements.cfm/att_228272_EN_TDAT14001ENN.pdf. Accessed May 2014
9. Uchiyama N, Matsuda S, Kawamura M, Kikura-Hanajiri R, Goda Y (2014) Identification of two new-type designer drugs, a piperazine derivative MT-45 (I-C6) and a synthetic peptide Noopept (GVS-111), with a synthetic cannabinoid A-834735, a cathinone derivative 4-methoxy-α-PVP and a phenethylamine derivative 4-methylbuphedrine from illegal products. Forensic Toxicol 32:9–18
10. Uchiyama N, Shimokawa Y, Matsuda S, Kawamura M, Kikura-Hanajiri R, Goda Y (2014) Two new synthetic cannabinoids, AM-2201 benzimidazole analog (FUBIMINA) and (4-methylpiperazin-1-yl)(1-pentyl-1*H*-indol-3-yl)methanone (MEPIRAPIM), and three phenethylamine derivatives, 25H-NBOMe 3,4,5-trimethoxybenzyl analog, 25B-NBOMe, and 2C-N-NBOMe, identified in illegal products. Forensic Toxicol 32:105–117
11. Uchiyama N, Matsuda S, Kawamura M, Shimokawa Y, Kikura-Hanajiri R, Aritake K, Urade Y, Goda Y (2014) Characterization of four new designer drugs, 5-chloro-NNEI, NNEI indazole analog, α-PHPP and α-POP, with 11 newly distributed designer drugs in illegal products. Forensic Sci Int 243:1–13
12. Uchiyama N, Kawamura M, Kikura-Hanajiri R, Goda Y (2013) URB-754: a new class of designer drug and 12 synthetic cannabinoids detected in illegal products. Forensic Sci Int 227:21–32
13. Frost JM, Dart MJ, Tietje KR, Garrison TR, Grayson GK, Daza AV, El-Kouhen OF, Yao BB, Hsieh GC, Pai M, Zhu CZ, Chandran P, Meyer MD (2010) Indol-3-ylcycloalkyl ketones: effects of N1 substituted indole side chain variations on CB2 cannabinoid receptor activity. J Med Chem 53:295–315
14. Buchler IP, Hayes MJ; Hegde SG, Hockerman SL, Jones DE, Kortum SW, Rico JG, Tenbrink RE, Wu KK (2009) Indazole derivatives as CB1 receptor modulators and their preparation and use in treatment of diseases. Patent: WO/2009/106980 September, 2009
15. Iversen L, Gibbons S, Treble R, Sedtola V, Huang X-P, Rolth BL (2013) Neurochemical profiles of some novel psychoactive substances. Eur J Pharmacol 700:147–151
16. Advisory Council on the Misuse of Drugs (ACMD) (2013) Benzofurans: a review of the evidence of use and harm. ACMD, London. https://www.gov.uk/government/uploads/system/uploads/attachment_data/file/261783/Benzofuran_compounds_report.pdf. Accessed May 2014
17. Power JD, Scott KR, Gardner EA, Curran McAteer BM, O'Brien JE, Brehon M, Talbot B, Kavanagh PV (2014) The syntheses, characterization and in vitro metabolism of nitracaine, methoxypiperamide and mephtetramine. Drug Test Anal. doi:10.1002/dta.1616
18. Nakachi N, Kiuchi Y, Inagaki M, Inazu M, Yamazaki Y, Oguchi K (1995) Effects of various dopamine uptake inhibitors on striatal extracellular dopamine levels and behaviors in rats. Eur J Pharmacol 281:195–203
19. Berger ML, Schweifer A, Rebernik P, Hammerschmidt F (2009) NMDA receptor affinities of 1,2-diphenylethylamine and 1-(1,2-diphenylethyl)piperidine enantiomers and of related compounds. Bioorg Med Chem 17:3456–3462
20. Kikura-Hanajiri R, Uchiyama N, Kawamura M, Goda Y (2014) Changes in the prevalence of new psychoactive substances before and after the introduction of the generic scheduling of synthetic cannabinoids in Japan. Drug Test Anal. doi:10.1002/dta.1584

Development/Plasticity/Repair

Microglia Enhance Neurogenesis and Oligodendrogenesis in the Early Postnatal Subventricular Zone

Yukari Shigemoto-Mogami,[1] Kazue Hoshikawa,[1] James E. Goldman,[2] Yuko Sekino,[1] and Kaoru Sato[1]

[1]Laboratory of Neuropharmacology, Division of Pharmacology, National Institute of Health Sciences, Tokyo 158-8501, Japan, and [2]Department of Pathology and Cell Biology, Columbia University College of Physicians and Surgeons, New York, New York 10032

Although microglia have long been considered as brain resident immune cells, increasing evidence suggests that they also have physiological roles in the development of the normal CNS. In this study, we found large numbers of activated microglia in the forebrain subventricular zone (SVZ) of the rat from P1 to P10. Pharmacological suppression of the activation, which produces a decrease in levels of a number of proinflammatory cytokines (i.e., IL-1β, IL-6, TNF-α, and IFN-γ) significantly inhibited neurogenesis and oligodendrogenesis in the SVZ. *In vitro* neurosphere assays reproduced the enhancement of neurogenesis and oligodendrogenesis by activated microglia and showed that the cytokines revealed the effects complementarily. These results suggest that activated microglia accumulate in the early postnatal SVZ and that they enhance neurogenesis and oligodendrogenesis via released cytokines.

Key words: cytokine; microglia; neurogenesis; neurosphere; oligodendrogenesis; subventricular zone

Introduction

CNS microglia have long been considered as resident immune cells, which are activated in response to pathological events. In pathological conditions, they change their morphology to an amoeboid shape, acquiring activation-specific phenotypes, such as chemotaxis, phagocytosis, and secretion of inflammatory cytokines (Nakajima and Kohsaka, 2001; Inoue, 2008; Monji et al., 2009; Kettenmann et al., 2011). However, microglia also have physiological roles in the normal CNS. They actively survey their territory with fine processes and receive stimuli from the environment as sensor cells (Kettenmann et al., 2011). *In vivo* lineage tracing studies have established that microglia differentiate from primitive myeloid progenitors that arise before embryonic day 8 and are identified in the CNS parenchyma even before definitive hematopoiesis (Ginhoux et al., 2010), whereas it has also been shown that microglia migrate from the lateral ventricle into the brain via the subventricular zone (SVZ) in the postnatal brain (Mohri et al., 2003). In the early embryonic brain, most microglia adopt an amoeboid morphology and characteristics of an activated form (Hirasawa et al., 2005). Microglia in the embryonic SVZ limit the production of cortical neurons by phagocytosing neural precursor cells (Cunningham et al., 2013). The number of microglia in the brain reaches a maximum during the early postnatal weeks (Wu et al., 1993; Xu and Ling, 1994), after which they transform into cells with a ramified shape, the typical morphology observed in the adult CNS (Ignácio et al., 2005). However, microglia are densely populated in neurogenic niches, such as the SVZ (Mosher et al., 2012), and appear more activated in the adult SVZ than in non-neurogenic zones (Goings et al., 2006). These developmental changes in the activation and the distribution of microglia strongly suggest that microglia play important roles in CNS development. However, the developmental dynamics of microglia in the postnatal SVZ and their roles in neurogenesis and gliogenesis at this stage are not well understood. We have examined the distribution and morphology of microglia in the rat forebrain during the neonatal-early postnatal period in detail and found a large number of active forms within the SVZ from P1 to P10, which then transformed from an activated form to a ramified form after P14. We here present evidence that microglia in the early postnatal SVZ promote both neurogenesis and oligodendrogenesis and that cytokines are important in these effects. To our knowledge, this is the first report showing a novel physiological function of microglia regulating neurogenesis and oligodendrogenesis in the early postnatal brain.

Received April 15, 2013; revised Dec. 21, 2013; accepted Dec. 27, 2013.

Author contributions: K.S. designed research; Y.S.-M., K.H., and K.S. performed research; Y.S.-M., K.H., J.E.G., Y.S., and K.S. analyzed data; Y.S.-M., J.E.G., Y.S., and K.S. wrote the paper.

This work was supported in part by a Grant-in-Aid for Young Scientists from MEXT, Japan (KAKENHI 21700422), the Program for Promotion of Fundamental Studies in Health Sciences of NIBIO, Japan, a Health and Labor Science Research Grant for Research on Risks of Chemicals, a Labor Science Research Grant for Research on New Drug Development from the MHLW, Japan to K.S., and a Health and Labor Science Research Grant for Research on Publicly Essential Drugs and Medical Devices, Japan to Y.S.

The authors declare no competing financial interests.

This article is freely available online through the *J Neurosci* Author Open Choice option.

Correspondence should be addressed to Dr. Kaoru Sato, Laboratory of Neuropharmacology, Division of Pharmacology, National Institute of Health Sciences, Kamiyoga 1-18-1, Setagaya-ku, Tokyo 158-8501, Japan. E-mail: kasato@nihs.go.jp.

DOI:10.1523/JNEUROSCI.1619-13.2014

 0270-6474/14/342231-13$15.00/0

Materials and Methods

Animals and treatment. All animals were treated in accordance with the guidelines for the Care and Use of Laboratory Animals of the Animal Research Committee of the National Institute of Health Sciences and followed the *Guide for the Care and Use of Laboratory Animals*. All experiments were approved by the Animal Research Committee of National Institute of Health Sciences and conformed to the relevant regulatory standards. The Wistar rats were purchased from Japan SLC and maintained under specific pathogen-free conditions at a controlled temperature and humidity and on a 12 h light/12 h dark cycle and had *ad libitum*

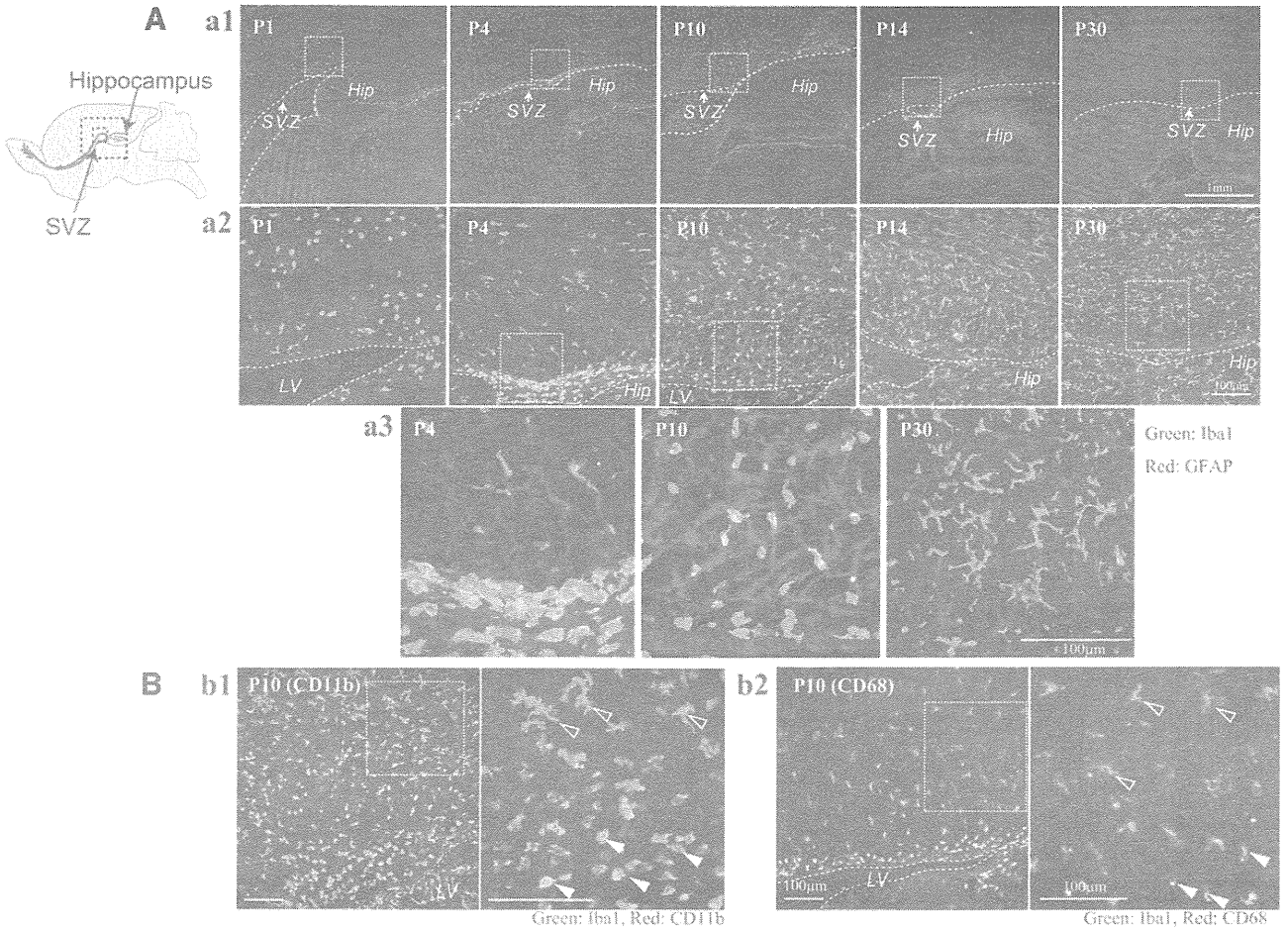

Figure 1. There is a population of activated microglia accumulated in the early postnatal SVZ. ***Aa1***, Distribution of microglia in the postnatal VZ/SVZ (P1, P4, P10, P14, P30). Sagittal sections of forebrains were immunostained with anti-Iba1 (green: microglia) and anti-GFAP antibodies (red: neural stem cells and astrocytes). ***Aa2***, Magnified images of the hatched squares in ***Aa1***. The accumulation in the SVZ in P4 and P10 was distinctive. ***Aa3***, Magnified images of the hatched squares in ***Aa2***. Morphological changes of microglia with age from amoeboid shape to more ramified shape is remarkable (P4, P10, P30). ***Bb1***, Activation of microglia in P10 SVZ. Sagittal sections immunostained with anti-CD11b (red: activated microglia) and anti-Iba1 antibodies (green: microglia). Right panel, Magnified image of the hatched square in the left panel. The microglia in the SVZ have an amoeboid shape and positive for CD11b (white arrowheads), whereas those outside SVZ have more ramified shape and are negative for CD11b (black arrowheads). ***Bb2***, Sagittal sections immunostained with anti-CD68 (red: activated microglia) and anti-Iba1 antibodies (green: microglia). Right panel, Magnified image of the hatched square in the left panel. The microglia in the SVZ have an amoeboid shape and positive for CD68 (white arrowheads), whereas those outside SVZ have more ramified shape and are negative for CD68 (black arrowheads). Similar results were obtained in three independent experiments.

access to food and water. Minocycline (30 mg/kg) or the same volume of PBS was injected into rats of either sex intraperitoneally for 3 d from postnatal day 2 (P2). Six hours after the last injection, rats were deeply anesthetized and the brains were removed on ice.

Immunohistochemistry (sagittal sections). Rats (P1, P4, P10, P14, P30) were anesthetized and then perfused with saline followed by 4% PFA, and then the brains were removed. From each half brain, sagittal sections were cut laterally at a thickness of 30 μm beginning 2 mm lateral from the midline. The sections were incubated for 2 h at room temperature in a blocking solution (3% normal goat serum, 0.3% Triton X-100 in PBS) and incubated for 24 h at 4°C in the solution, including the primary antibodies (rabbit anti-Iba1 antibody [019–9741, Wako; 1:500], mouse anti-GFAP antibody [MAB3402, Millipore; 1:200], mouse anti-rat CD11b antibody [MAB1405, AbD Serotec; 1:100], anti-rat CD68 antibody [MCA341R, AbD Serotec; 1:100], rabbit anti-Ki-67 [SP6, M3061, Spring Bioscience; 1:10], anti-nestin antibody [MAB353, Millipore; 1:100], goat anti-doublecortin [Dcx] antibody [sc-8066, Santa Cruz Biotechnology; 1:200], goat anti-PDGFRα antibody [sc-31178, Santa Cruz Biotechnology; 1:50], anti-oligodendrocyte marker O1 [O1] antibody [MAB344, Millipore, 1:50], mouse anti-MBP antibody [MAB 382, Millipore; 1:50], rabbit anti-ALDH1L1 antibody-astrocyte marker antibody [ab87117, Abcam; 1:1000], mouse anti-S100β antibody [S2532, Sigma; 1:100], rabbit anti IGF-1 antiserum [GroPep Biotechnology; [1:200]). After incubation, the sections were washed and incubated for 3 h at room temperature in the solution, including the secondary antibodies (anti-rabbit IgG-conjugated Alexa Fluorochrome or anti-mouse IgG-conjugated Alexa Fluorochrome [Invitrogen; 1:1000]). The stained sections were analyzed using a Nikon A1R-A1 confocal microscope system. To count the number of cells positive for each differentiation marker, 613 × 613 μm^2 and 1024 × 1024 μm^2 squares were set on both sides of the fornix. The cell numbers in the two squares were counted and averaged for the cell numbers in one section. The averaged data of 3 sections at 90 μm intervals were treated as the data of one animal and the data from 6 animals were statistically analyzed.

Immunohistochemistry (coronal sections). Three points on the skull at three different rostrocaudal stereotaxic coordinates (i.e., anterior, middle, posterior) were marked with animal tattoo ink (Ketchum) at P1. These three points with different rostrocaudal levels were determined according to a previous report (Suzuki and Goldman, 2003): rostral point: 2 mm anterior, 1 mm lateral to the bregma; middle point: 0.7 mm anterior, 1 mm lateral to the bregma; caudal point: 0.5 mm posterior, 1 mm lateral to the bregma. Then the animals were perfused at P1, P3, P10, and P30, and the brains were removed as described above. From each half brain, coronal sections were cut at each marked point from anterior to posterior. The sections were immunostained with anti-Iba1 and anti-CD68 as described above. After immunostaining, the sections were coun-

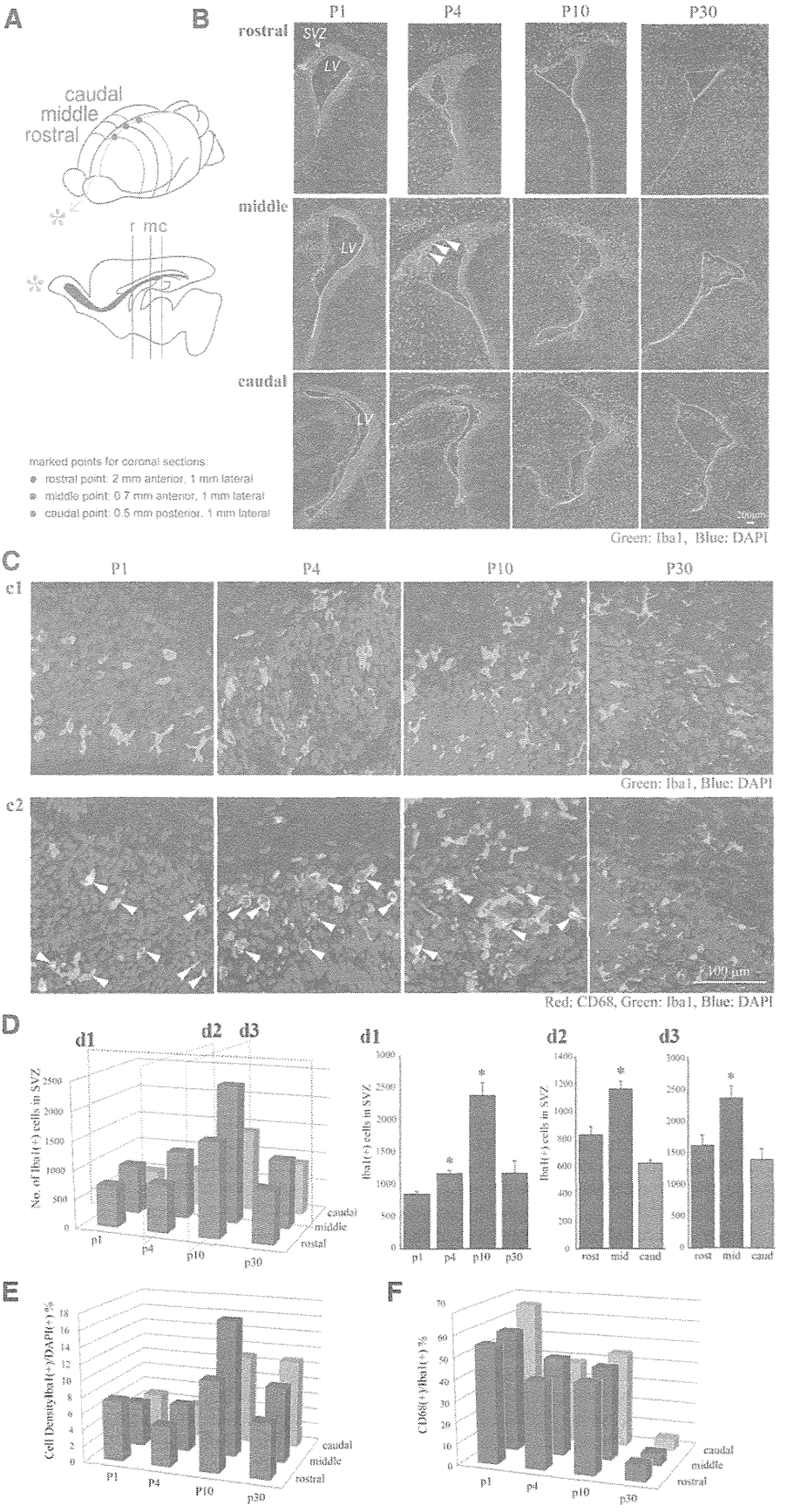
A
B
caudal
middle
rostral
r mc
marked points for coronal sections:
rostral point: 2 mm anterior, 1 mm lateral
middle point: 0.7 mm anterior, 1 mm lateral
caudal point: 0.5 mm posterior, 1 mm lateral
P1
P4
P10
P30
rostral
middle
caudal
SVZ
LV
200μm
Green: Iba1, Blue: DAPI
C
c1
c2
Green: Iba1, Blue: DAPI
Red: CD68, Green: Iba1, Blue: DAPI
100 μm
D
d1
d2
d3
No. of Iba1(+) cells in SVZ
Iba1(+) cells in SVZ
p1
p4
p10
p30
rost
mid
caud
E
F
Cell Density Iba1(+)/DAPI(+) %
CD68(+)/Iba1(+) %

terstained with DAPI (1:500; Invitrogen) for 30 min to visualize the SVZ. The cell numbers of microglia (Iba1 $^+$) and activated microglia (Iba1 $^+$ CD68 $^+$) in the SVZ (the region with dense DAPI signals) were counted in one section. The averaged data of three sections at 90 μm intervals across the marked points were treated as the data for each rostrocaudal level. The data from 6 to 9 hemispheres per one rostrocaudal level were statistically analyzed.

Western blotting. P4 Wistar rat brains were cut into sagittal sections. Under a microscope, a parasagittal section (from 1 mm lateral, 2 mm thickness) was taken from each half brain and meninges were carefully removed. The VZ/SVZ was identified by its slightly darker, more transparent appearance compared with the overlying corpus callosum. We cut out the VZ/SVZ between 0.4 mm anterior and 3 mm posterior (posterior end of SVZ) from bregma so as not to include the rostral migratory stream. Dissected VZ/SVZ tissues were homogenized on ice in extraction buffer (20 mM Tris, 2 mM EDTA, 0.5 mM EGTA, 0.32 M sucrose, protease inhibitor mixture), and centrifuged at 1000 × *g* for 10 min. Proteins in the lysates were resolved with SDS-PAGE and transferred to PVDF membranes. The membranes were incubated overnight in BlockAce blocking solution at 4°C. Then the membranes were incubated with primary antibodies (anti-CD11b [1:1000], anti-CD68 [1:2000], anti-nestin [1:1000], anti-PDGFRα [1:200], anti-ALDH1L1 [1:1000], anti-S100β [1:2000]) for 1 h at 25°C. After washing three times, the membranes were incubated with HRP-conjugated anti-rabbit or anti-mouse antibody (1:5000) for 1 h at 25°C. The membranes were then washed three times and signals were visualized by chemiluminescence detectors LAS3000 (Fuji film).

Measurement of cytokine levels. Cytokine levels in the SVZ were determined with Bio-Plex cytokine analysis system (Bio-Rad Laboratories). Tissue lysates of VZ/SVZ fractions were obtained from rats at P1, P4, P10, and P30 as described in Western blotting. The concentrations of Il-1α, Il-1β, IL-2, IL-4, IL-6, Il-10, GM-CSF, IFN-γ, and TNF-α were measured by the Bio-Plex rat cytokine 9 plex kit according to the manufacturer's instruction. In some cases, IGF-1, Il-1β IL-6, TNF-α, and IFN-γ concentrations were measured by ELISA kit according to the manufacturer's instruction. The protein levels of tissue lysates were measured by BCA protein assay. The amount of each cytokine in 100 μg of total protein is shown for comparison. To determine the cytokine release from activated microglia *in vitro*, microglia were activated by LPS (10 ng/ml) in the presence or absence of minocycline (10 μM) for 30 min and washed carefully and incubated in the normal medium for 24 h. After 24 h incubation, the cell culture supernatants were collected, and concentration of Il-1β, IL-6, IFN-γ, and TNF-α were measured by ELISA kit.

Cell culture: neurosphere culture. Rat neural stem cells were cultured as previously described (Reynolds et al., 1992; Hamanoue et al., 2009) with slight modifications. Briefly, telencephalons were dissected from embryonic day 16 (E16) rats of either sex in ice-cold DMEM/F12, minced, and dispersed into single cells by pipetting. Cells were then cultured in DMEM/F12 containing B27 supplement (×200), 20 ng/ml FGF2, and 20 ng/ml EGF for 7 d. The primary neurospheres and single cells were differentiated in growth factor-free medium in glass chambers coated with ornithine/fibronectin. In some cases, primary neurosphere were incubated with TrypLE Select for 15 min and dissociated by pipetting. Single cells were differentiated in glass chambers coated with polyornithine/laminin.

Microglia culture. Rat microglia were cultured as previously described (Nakajima et al., 1992). In brief, mixed glial cultures were prepared from the cerebral cortex of P1 Wistar rats and maintained for 12–23 d in DMEM containing 10% FBS. The floating microglia over the mixed glial cultures were collected and transferred to appropriate dishes or transwells.

Neural stem cell differentiation assay. To examine the effects of activated microglia on neural development and the contribution of cytokines to the effects, we used modified cocultures of neurospheres with activated microglia. Microglia cultured independently of neurospheres on transwells were activated by LPS (10 ng/ml) in the presence or absence of minocycline (10 μM) for 30 min and washed carefully to prevent residual LPS and minocycline. The transwells on which microglia were cultured were set on the neurospheres 1 d after the starting point of the differentiation and incubated for differentiation periods suitable for neurons (7 d) or oligodendrocytes (11 d). In some cases, we performed the coculture of cells dissociated from neurospheres and activated microglia. To check the effects of minocycline alone, these cells were incubated in the presence of minocycline (10 μM) for 7 d. Neurospheres and single neural stem cells were immunohistochemically stained for β3-tubulin, PDGFRα, O4, GFAP, and TOTO3 according to the manufacture's instruction (Stem Cell Kits, R&D Systems). To examine the effects of function-blocking antibodies on differentiation, the neurospheres were differentiated in the presence of function-blocking antibodies (goat anti-rat IL-1β antibody [AF-501-NA, R&D Systems], goat anti-rat IL-6 antibody [AF-506, R&D Systems], TNF-α antibody [70R-TR007X, Fitzgerald], and goat anti-mouse/rat IFN-γ antibody [AF-585-NA, R&D Systems]) (1 μg/ml for each). The effects of these function-blocking antibodies were compared with the same concentration of isotype-matched control IgG: normal goat IgG control [AB-108-C, R&D Systems] and rabbit IgG control [31R-AR001, R&D Systems] (1 μg/ml for each). The effect of the mixture of function blocking antibodies (goat anti-rat IL-1β antibody, goat anti-rat IL-6 antibody, TNF-α antibody, and goat anti-mouse/rat IFN-γ antibody, 1 μg/ml for each) was compared with the control, which included same concentrations of isotype-matched control IgGs (i.e., 3 μg/ml of normal goat IgG control and 1 μg/ml of rabbit IgG control). To examine the effects of a single cytokine, the neurospheres were differentiated in the presence of each individual recombinant cytokine (rIL-1β, rIL-6, rTNF-α, and rIFN-γ at 1 or 10 ng/ml). After the differentiation period, the cells were stained immunocytochemically as described above.

Data analysis and statistics. All data are shown as the mean ± SEM. Statistical analysis was performed using Student's *t* test, or Tukey's test by ANOVA. Differences were considered to be significant at $p < 0.05$.

Materials. Minocycline, LPS, anti-S100β antibody (S2532), and EGF were purchased from Sigma. Bio-Plex rat cytokine 9 plex was purchased from Bio-Rad Laboratories. Recombinant cytokines (rIL-1β, rIL-4, rIL-6, rIFN-γ, rTNF-α) and FGF2 were purchased from PeproTech. Maximum sensitivity substrate and BCA protein assay were purchased from Thermo Scientific. CanGet Signals was purchased from Toyobo. HRP-conjugated anti-rabbit, mouse antibodies were purchased from GE Healthcare Life Science. DAPI, TOTO3, anti-mouse, sheep, rabbit IgG, and anti-mouse IgM-conjugated AlexaFluor were purchased from Invitrogen. BlockAce was purchased from DS Pharma Biomedical. B27 supplement, TrypLE Serect, FBS, and DMEM were purchased from Invitrogen.

←

Figure 2. The temporal and spatial dynamics of activated microglia in the postnatal SVZ. ***A***, A schematic of the rostrocaudal levels in this experiment. ***B***, The distribution of microglia in the rostral, medial, and caudal SVZ at P1, P4, P10, and P30. Coronal sections of forebrains at rostral (2 mm anterior to the bregma), medial (0.7 mm anterior to the bregma), and caudal (0.5 mm posterior to the bregma) levels were immunostained with anti-Iba1 (green: microglia) followed by DAPI staining (blue: cell nuclei). A population of activated microglia accumulated within the SVZ at P1-P10. ***Cc1***, Typical morphology of microglia in the middle SVZ at P1, P4, P10, and P30. Morphological change of microglia with age from amoeboid shape to more ramified shape is remarkable. ***Cc2***, The middle SVZ sections immunostained with anti-CD68 (red: activated microglia) and anti-Iba1 antibodies (green: microglia). The microglia at P1, P4, and P10 in the SVZ have an amoeboid shape and are positive for CD68 (representative cells: white arrowheads), whereas those at p30 have a more ramified shape and are negative for CD68. ***D***, The quantification of the number of Iba1 $^+$ cells in the SVZ. ***d1***, Time course of the Iba1 $^+$ microglia in the middle SVZ. The number peaked at P10. d2, d3, The comparison of the numbers of microglia among the rostral, middle, and caudal SVZ at P4 (***d2***) and P10 (***d3***). $^*p < 0.05$ versus p1 or rost group (Tukey's test by ANOVA). Data are mean ± SEM. ***E***, The cell density of Iba1 $^+$ microglia at different rostrocaudal levels at P1, P4, P10, and P30. The cell density of microglia in the SVZ paralleled with that of the number of microglia throughout a period of the observation. ***F***, The ratio of activated microglia in the SVZ (CD68 $^+$/Iba1 $^+$). During the experimental period, the highest ratio was obtained at P1. We confirmed the similar results in three independent experiments.

Results

We first investigated the distribution of microglia in the postnatal rat forebrain (Figs. 1 and 2). Sagittal sections were immuno-

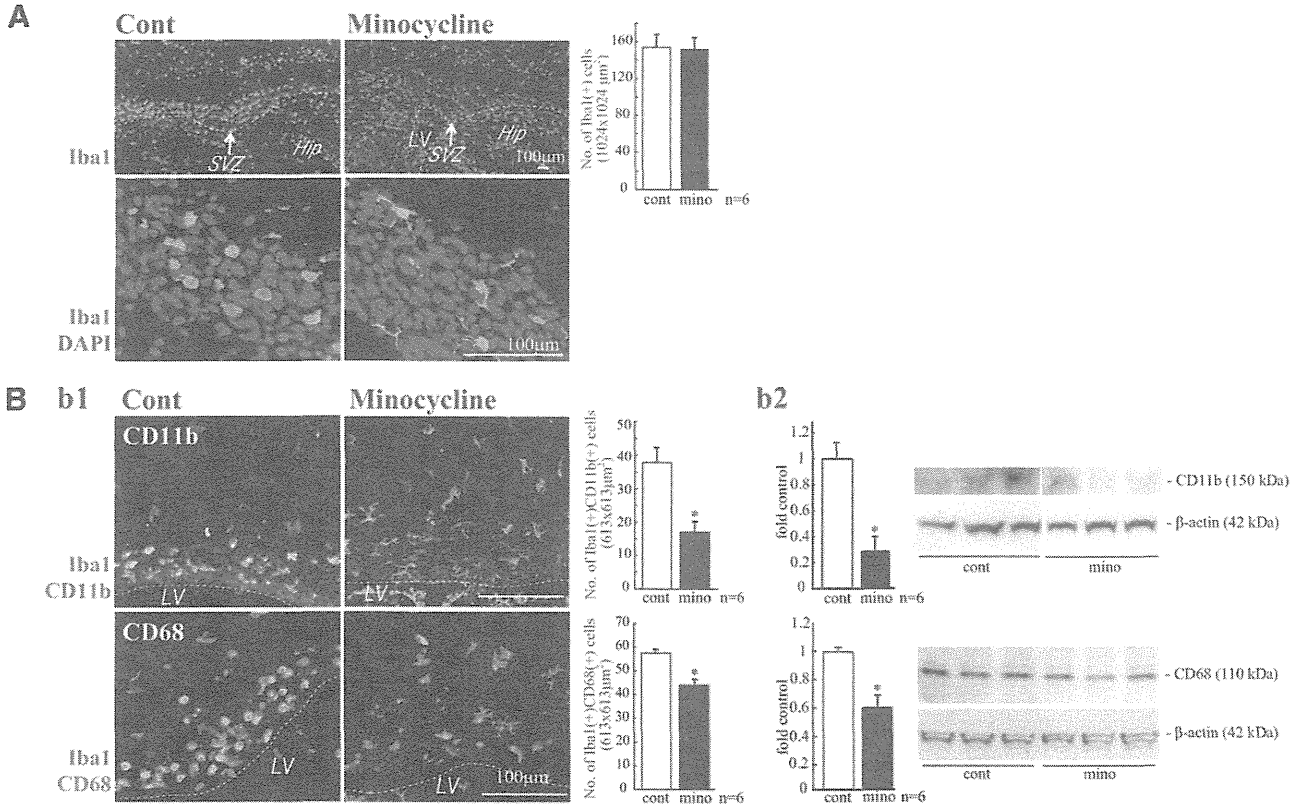

Figure 3. Minocycline suppressed microglial activation *in vivo*. ***A***, Effects of minocycline on the number of Iba1 $^{+}$ cells in the SVZ and their morphologies. Minocycline was administered by intraperitoneal injection for 3 d beginning at P2 (30 mg/kg/d, P2-P4, $n = 6$/group). Sagittal sections of minocycline-treated forebrains were immunostained for Iba1 (green) followed by DAPI staining (cyan). Although the number of Iba1 $^{+}$ microglia in the SVZ did not change (graph), their shape shifted from an amoeboid type to a more ramified type by minocycline (bottom). ***Bb1***, Effects of minocycline on the expression of activation markers and the morphologies of microglia. Sagittal sections of minocycline-treated forebrains were immunostained for Iba1 (green), and CD11b (red), and CD68 (red). Minocycline significantly decreased the number of cells positive for CD11b or CD68. The morphologies of the cells were also changed from amoeboid shape to more ramified shape. ***Bb2***, The significant decrease in the expression of CD11b and CD68 was confirmed by Western blotting of the SVZ as well. $^{*}p < 0.05$ (Student's *t* test). Data are mean ± SEM. Similar results were obtained in three independent experiments.

stained with anti-Iba1, the marker for all microglia (green: microglia), and anti-GFAP antibodies (red: neural stem cells and astrocytes) at P1, P4, P10, P14, and P30. We found that a large number of microglia accumulated in the postnatal SVZ from P1 to P10 (Fig. 1*A*), especially at P4. The microglia in the VZ/SVZ at P1 and P4 display an amoeboid shape, whereas those outside the SVZ have a more ramified shape (Fig. 1*Aa2*). At P10, the number of microglia outside the SVZ had dramatically increased; the microglia in the VZ/SVZ remained amoeboid. At P14, the number of microglia had increased further and now ramified microglia were also observed in the VZ/SVZ. At P30, the numbers of microglia in the SVZ had decreased and most of the microglia had assumed a ramified shape. Further magnified images in Figure 1*Aa3* show that the shape of microglia in the SVZ changed gradually from amoeboid (P4) to ramified (P30). Figure 1*B* shows the expression of CD11b (Fig. 1*Bb1*) and CD68 (Fig. 1*Bb2*) in the SVZ microglia at P10. CD11b is potentially a marker for all microglia; however, its level is highly elevated by activation. CD68 is a marker for activated microglia. The levels of CD11b and CD68 are much higher in the amoeboid microglia in the SVZ (white arrowheads) than in the ramified ones outside the SVZ (black arrowheads), indicating that the SVZ amoeboid microglia have an activated phenotype.

To examine the developmental dynamics of microglia in the SVZ temporally and spatially, we examined the distribution of microglia in coronal sections that include rostral, medial, and caudal SVZ at P1, P4, P10, and P30 (Fig. 2). Each rostrocaudal level was determined according to a previous report (Suzuki and Goldman, 2003). Coronal sections were immunostained with anti-Iba1 (green: microglia) followed by DAPI staining (blue: cell nuclei) (Fig. 2*B*,*C*). The SVZ could be clearly delineated by its dense cellularity. From P1 to P10, a large number of microglia accumulated at all rostral, middle, and caudal levels. When we quantified the number of microglia in the SVZ, they gradually increased from P1 to P10, reached a maximum at p10, and decreased at P30 at all coronal levels (Fig. 2*B*,*D*, d1). Microglia displayed an amoeboid shape at P1, P4, and P10 but had become more ramified at P30 (Fig. 2*Cc1*). Among the different rostrocaudal levels, the number of microglia in the middle SVZ was significantly larger than in other levels at all ages (Fig. 2*D*, d2, d3). The changes in cell density (i.e., the ratio of Iba1 $^{+}$/DAPI $^{+}$) of microglia in the SVZ paralleled that of the number of microglia throughout the period of observation (Fig. 2*E*). We next examined immunostaining for CD68 in SVZ microglia. Figure 2*Cc2* shows representative images of double staining with anti-Iba1 and anti-CD68. At P1 and P4, most Iba1+ microglia in the SVZ were also positive for CD68. At P4, the CD68 signals became much stronger. At P10, a few microglia had appeared that had little CD68. At P30, double-positive cells were markedly decreased in number. The time course of the ratio of CD68 $^{+}$/Iba1 $^{+}$ cells is shown in Figure 2*F*: the highest ratio was obtained at P1. The ratios at P4 and P10 were almost equivalent and then were

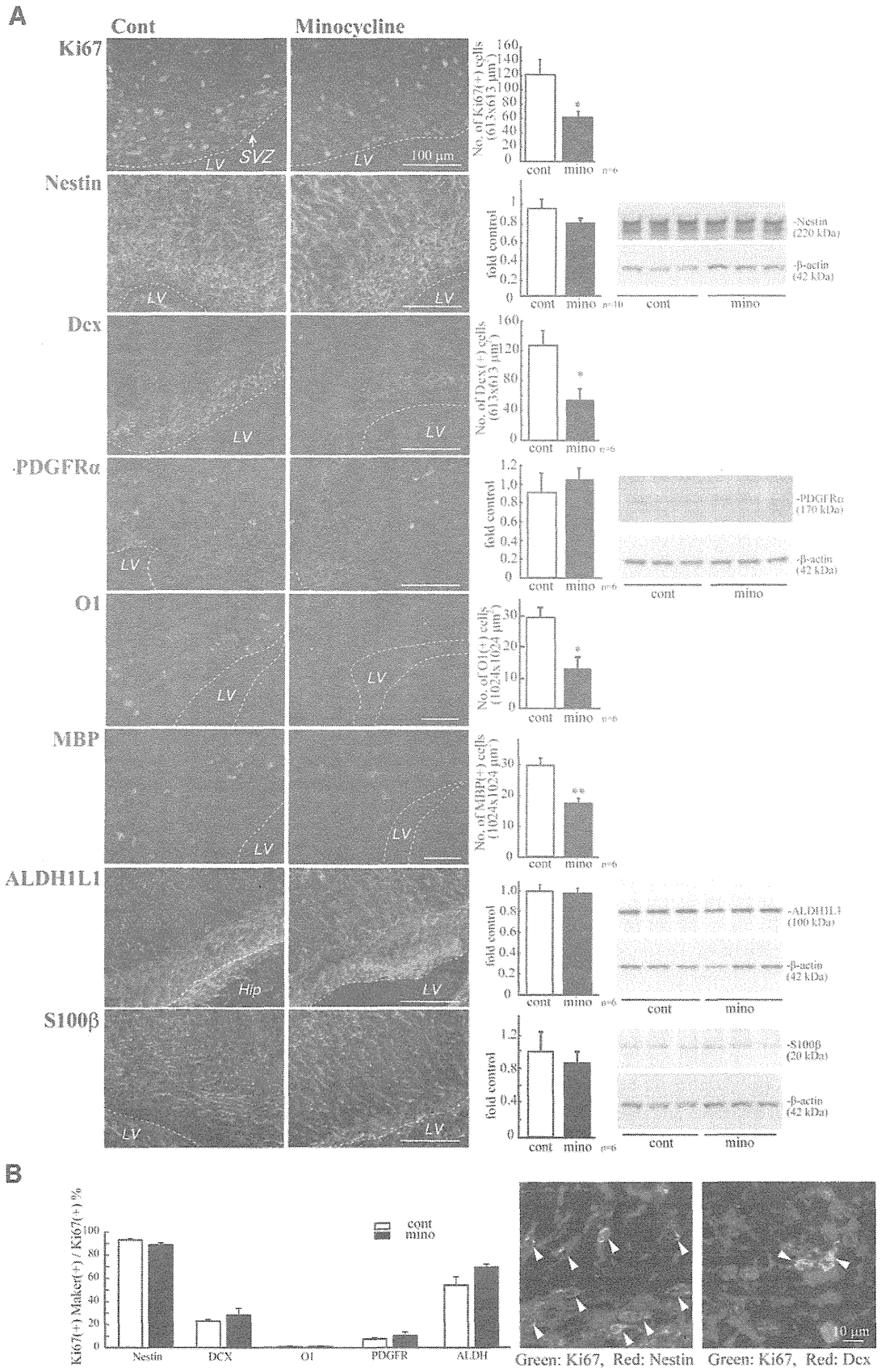

Figure 4. Minocycline decreased the numbers of proliferating cells, neuronal progenitors, and oligodendrocyte progenitors in the early postnatal SVZ. ***A***, Minocycline was administered by intraperitoneal injection for 3 d beginning at P2 (30 mg/kg/d, P2-P4, $n = 6$/group). Sagittal sections of forebrains were immunostained with antibodies to Ki67, nestin, Dcx, PDGFRα, O1, MBP, ALDH1L1, and S100β. The numbers of cells positive for Ki67, Dcx, MBP, or O1 were counted, whereas the protein levels of nestin, PDGFRα, ALDH1L1, and S100β (*Figure legend continues.*)

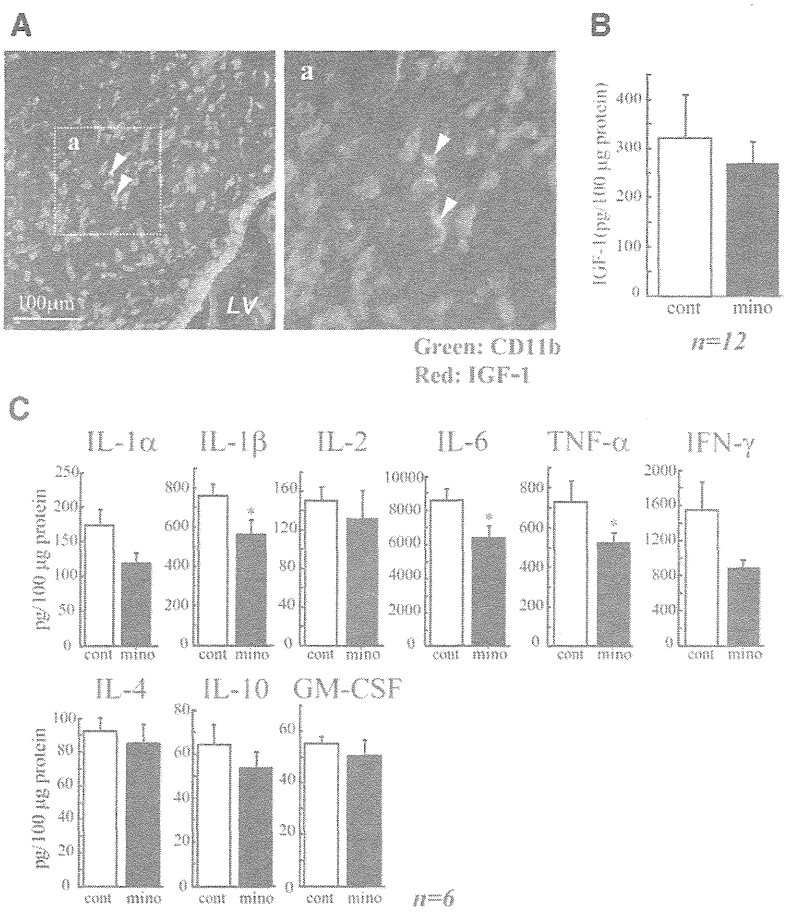

Figure 5. The activated microglia raised the cytokine levels in the SVZ. ***A***, A subpopulation of the microglia express IGF-1 in the early postnatal SVZ, but IGF-1 is not involved in the action of activated microglia during this period. Sagittal sections were immunostained with anti-CD11b (green: microglia) and anti IGF-1 (red) antibodies. Right panel, Magnified image of the square in the left. A subpopulation of microglia is positive for IGF-1 (arrowheads). The percentage of CD11b $^+$IGF-1 $^+$ was 43.42 ± 6.72% in CD11b $^+$ cells. ***B***, Minocycline did not affect the amount of IGF-1 in the early postnatal SVZ. Minocycline was administered by intraperitoneal injection for 3 d beginning at P2 (30 mg/kg/d, P2-P4, n = 6/group), and the amount of IGF-1 in the SVZ was quantified by ELISA. ***C***, Minocycline decreased the amount of inflammatory cytokines in the SVZ. IL-1α, IL-1β, IL-2, IL-4, IL-6, IL-10, GM-CSF, IFN-γ, and TNF-α levels in the SVZ tissue lysate were measured by BioPlex cytokine detection assay system. $^*p <$ 0.05 (Student's t test). n = 6 rats/group. Data are mean ± SEM. Similar results were obtained in two independent experiments.

remarkably decreased at P30. These results are consistent with those obtained from the sagittal sections (Fig. 1), showing the population of activated microglia that accumulated within the SVZ during the early postnatal period.

We therefore examined the specific roles of these microglia in the early postnatal SVZ. At early postnatal ages, both neurogenesis and gliogenesis are active in the SVZ (Gould et al., 1999; Wagner et al., 1999; Doetsch and Scharff, 2001; Zerlin et al., 2004; Marshall et al., 2008). To suppress the activation of microglia, we used minocycline, a tetracycline antibiotic, long used to suppress microglial activation (Tikka et al., 2001; Zhao et al., 2007). We first verified the effects of minocycline on the activation of microglia. Minocycline was administered by intraperitoneal injection for 3 d beginning at P2 (30 mg/kg/d, P2-P4, n = 6/group), and sagittal sections of minocycline-treated rat forebrains were immunostained for Iba1, CD11b, and CD68. Minocycline did not change the numbers of Iba1-positive microglia in the VZ/SVZ (Fig. 3*A*, top), but it dramatically changed their shape from amoeboid to more ramified (Fig. 3*A*, bottom). The number of CD11b $^+$ cells was significantly decreased (Fig. 3*Bb1*, top and graph), and the decrease in CD11b levels in the SVZ was confirmed by Western blotting (Fig. 3*Bb2*, top graph and photo). The number of CD68 $^+$ cells and the level of CD68 were also decreased (Fig. 3*B*, bottom data). These results indicate that our administration of minocycline suppresses the activation of SVZ microglia.

We then investigated the effects of minocycline on early postnatal differentiation. After the administration of minocycline, sagittal sections were immunostained with differentiation markers: Ki67 (proliferating cells), nestin (stem cells), Dcx (neuronal progenitors), PDGFRα (oligodendrocyte progenitors [polydendrocytes]), O1 (oligodendrocyte progenitors [premyelinating oligodendrocytes]), MBP (mature oligodendrocyte [premyelinating and myelinating oligodendrocytes] (Nishiyama et al., 2009), ALDH1L1 (astrocyte progenitors), and S100β $^+$ (astrocytes) (Fig. 4*A*). The numbers of cells positive for Ki67, Dcx, O1, and MBP were counted, whereas the levels of nestin, PDGFα, ALDH1L1, and S100β were examined by Western blotting because it was hard to discriminate the cell morphologies by these signals. Minocycline significantly decreased the number of Ki67 $^+$ cells and slightly decreased the level of nestin. The number of cells positive for Dcx was also significantly reduced. Furthermore, minocycline decreased the numbers of cells positive for O1 and MBP, whereas the numbers of PDGFRα $^+$ cells rather tended to increase. The levels of ALDH1L1 and S100β did not change. These results suggest that activated microglia in the early postnatal SVZ enhance neurogenesis and oligodendrogenesis, and activated microglia affect oligodendrocyte progenitors at rather later stage of differentiation. We also performed the double staining of Ki67 with the respective differentiation markers (Fig. 4*B*). Although the total number of Ki67 $^+$ cells was decreased by minocycline, consistent with Figure 4*A*, the percentage of Ki67 $^+$ cells also positive for the respective differentiation markers did not change in the absence or presence of minocycline (Fig. 4*B*, left graph), suggesting that minocycline did not affect the proliferation of progenitors of the specific cell types. Typical images of the SVZ cells positive for

←

(*Figure legend continued.*) were examined by Western blotting. Minocycline significantly decreased the number of Ki67 $^+$ proliferating cells and decreased the level of nestin. The number of cells positive for Dcx was significantly reduced. Minocycline decreased the numbers of cells positive for O1 and MBP, whereas the expression level of PDGFRα tended to increase. $^*p <$ 0.05, $^{**}p <$ 0.01 (Student's t test). n = 6 mice/group. Data are mean ± SEM. ***B***, The ratio of the Ki67 $^+$ cells also positive for respective differentiation markers did not change in the absence or presence of minocycline (left graph). Typical images of the cells positive for Ki67 and Nestin, and the cells positive for Ki67 and Dcx in the control group are shown (right panels). We confirmed the same results in three independent experiments.